

GLOW DISCHARGE DETECTORS (GDDS) FOR MILLIMETER-WAVE  
RADIATION DETECTION AND IMAGING

A THESIS SUBMITTED TO  
THE GRADUATE SCHOOL OF NATURAL AND APPLIED SCIENCES  
OF  
MIDDLE EAST TECHNICAL UNIVERSITY

BY

NAMIG ALASGARZADE

IN PARTIAL FULFILLMENT OF THE REQUIREMENTS  
FOR  
THE DEGREE OF MASTER OF SCIENCE  
IN  
PHYSICS

JANUARY 2018



Approval of the thesis:

**GLOW DISCHARGE DETECTORS (GDDS) FOR MILLIMETER-WAVE  
RADIATION DETECTION AND IMAGING**

submitted by **NAMIG ALASGARZADE** in a partial fulfillment of the requirements  
for the degree of **Master of Science in Physics Department, Middle East Technical  
University** by,

Prof. Dr. Gülbin Dural Ünver  
Dean, Graduate School of **Natural and Applied Sciences**

\_\_\_\_\_

Prof. Dr. Altuğ Özpineci  
Head of Department, **Physics**

\_\_\_\_\_

Assoc. Prof. Dr. Ilker Ümit Uzun-Kaymak  
Supervisor, **Physics Dept., METU**

\_\_\_\_\_

**Examining Committee Members:**

Prof. Dr. Nizami Hasanli  
Physics Department, METU

\_\_\_\_\_

Assoc. Prof. Dr. Ilker Ümit Uzun-Kaymak  
Physics Department, METU

\_\_\_\_\_

Prof. Dr. Hakan Altan  
Physics Department, METU

\_\_\_\_\_

Assoc. Prof. Dr. Asaf Behzat Şahin  
Electrical and Electronics Engineering Dept.,  
Ankara Yıldırım Beyazıt University

\_\_\_\_\_

Assoc. Prof. Dr. Alpan Bek  
Physics Department, METU

\_\_\_\_\_

**Date:** January 26<sup>th</sup>, 2018

**I hereby declare that all information in this document has been obtained and presented in accordance with academic rules and ethical conduct. I also declare that, as required by these rules and conduct, I have fully cited and referenced all material and results that are not original to this work.**

Name, Last Name: Namig Alasgarzade

Signature :

## **ABSTRACT**

### **GLOW DISCHARGE DETECTORS (GDDS) FOR MILLIMETER-WAVE RADIATION DETECTION AND IMAGING**

Alasgarzade, Namig

M.S., Department of Physics

Supervisor: Assoc. Prof. Dr. Ilker Ümit Uzun-Kaymak

January 2018, 58 pages

Commercially available indicator lamps, also known as Glow Discharge Detectors (GDDs), are employed for the purpose of millimeter wave radiation detection and imaging. Previous studies show that dominant radiation detection mechanism for GDDs is enhanced cascade ionization. The current-voltage characteristics of GDDs are obtained and working mode is found as abnormal glow mode. The plasma parameters such as electron temperature and gas composition inside GDDs are studied using Optical Emission Spectroscopy method. In order to employ a GDD as a pixel detector, a read-out electronics with an amplifier circuit is developed. This circuit is used to measure the changes in current of the plasma discharge. The detection performance of two different GDDs, namely N520A and N523, are tested at 82 GHz and 100 GHz radiation frequencies. The response of GDDs is found highly sensitive to the discharge current and polarization of the incident millimeter wave radiation. A continuous-wave imaging system is constructed using the GDD as a detector. The images are obtained at 82 GHz, 100 GHz and 119 GHz radiation frequencies.

**Keywords:** Glow Discharge Detector, Millimeter wave radiation, Voltage Current Characteristics, Optical Emission Spectroscopy.

## ÖZ

### MİLİMETRİK DALGA RADYASYON ALGILAMASI VE GÖRÜNTÜLEME İÇİN PARILTILI DEŞARJ DEDEKTÖRLERİ

Alasgarzade, Namig

Yüksek Lisans, Fizik Bölümü

Tez Yöneticisi: Doç. Dr. Ilker Ümit Uzun-Kaymak

Ocak 2018, 58 sayfa

Parıltılı deşarj dedektörleri (GDD) olarak da bilinen piyasada mevcut olan deşarj lambaları milimetrik dalga ışımasının algılanması ve görüntülenmesi amacıyla kullanılmıştır. Daha önce yapılan çalışmalar GDD' lerdeki baskın ışımaya algılama mekanizmasının kademeli iyonizasyonu çoğalttığını göstermiştir. GDD' lerin akım – voltaj karakteristikleri elde edilerek, çalışma modunun anormal parıltı modunda olduğu tespit edilmiştir. GDD' lerin içerisindeki elektron sıcaklığı ve gaz bileşimi gibi plazma parametreleri Optik Yayınım Spektroskopi yöntemi kullanılarak çalışılmıştır. Tek başına GDD' nin bir piksel dedektör olarak kullanılması için bir yükselteç devresi geliştirilmiştir. Bu devre kullanılarak plazma deşarj akımındaki değişimler ölçülmüştür. N520A ve N523 olarak isimlendirilen iki farklı GDD' lerin algılama performansları 82 GHz ve 100 GHz ışınım frekanslarında test edilmiştir. GDD' lerin deşarj akımına ve gelen milimetrik dalga ışımasının polarizasyonuna karşı yüksek hassasiyet gösterdiği bulunmuştur. GDD' nin dedektör olarak kullanıldığı sürekli dalgada çalışan bir görüntüleme sistemi kurulmuştur. Görüntüler 82 GHz, 100 GHz ve 119 GHz ışımaya frekanslarında elde edilmiştir.

**Anahtar Kelimeler:** Parıltılı Deşarj Dedektörü, Milimetrik Dalga Işıması, Akım – Voltaj Karakteristikleri, Optik Yayınım Spektroskopisi.

To my father and mother...

## ACKNOWLEDGMENTS

I am most grateful to my supervisor Assoc. Prof. Dr. Ilker Ümit Uzun-Kaymak for her assistance, guidance and understanding. I also appreciate her continuous support throughout my research and study.

I would like to express my thanks to Prof. Dr. Hakan Altan and Assoc. Prof. Dr. Asaf Behzat Şahin for their encouragement and sharing theoretical and experimental knowledge with me.

I want to thank to Doğan Mansuroğlu, Taylan Takan, Burcu Karagöz, Mehmet Ali Nebioğlu, Mirzamin Ağazade and Seher Fatma Alasgarzade for their friendship and support.

Finally, I would like to thank to my family for always encouraging me to finish my study and giving their support to my decisions in my life.

This work is supported under The Scientific and Technical Research Council of Turkey (TUBITAK) Grant #113F321 and partially under The Scientific and Technical Research Council of Turkey (TUBITAK) Grant #113E230. This research is sponsored in part by the NATO Science for Peace and Security Programme under grant MD.SFPP 984775.

## TABLE OF CONTENTS

ABSTRACT .....	v
ÖZ .....	vii
ACKNOWLEDGMENTS .....	x
TABLE OF CONTENTS .....	xi
LIST OF TABLES .....	xiii
LIST OF FIGURES .....	xiv
LIST OF ABBREVIATIONS .....	xviii
CHAPTERS .....	xviii
1. INTRODUCTION .....	1
2. THEORETICAL BACKGROUND .....	3
2.1. DC Glow discharge.....	3
2.1.1. Collisions in gas discharge.....	4
2.1.2. Electron emission from the electrode.....	6
2.1.3. Townsend Breakdown Process .....	7
2.1.4. Current-Voltage (I-V) Characteristics.....	9
2.1.5. Layers of the gas discharge .....	11
2.2. Optical Emission Spectroscopy .....	13
2.2.1. Measurements of the electron temperature .....	14
2.2.1.1. The line ratio method .....	14
2.2.1.2. The Boltzmann Plot method.....	15
2.2.2. Measurements of the electron density.....	16

2.3. GDD-Millimeter Wave Interaction.....	17
2.3.1. Response time of the Glow Discharge Detector .....	21
3. DESCRIPTION OF THE EXPERIMENTAL SETUPS .....	25
3.1. Plasma Characterization.....	25
3.1.1. Current-Voltage (I-V) Characteristics.....	25
3.1.2. Optical Emission Spectroscopy.....	27
3.2. GDD-Millimeter wave detection .....	28
3.3. GDD as a single pixel detector .....	32
4. EXPERIMENTAL RESULTS AND DISCUSSION .....	35
4.1. Plasma Characterization.....	35
4.1.1. Current-Voltage (I-V) Characteristics measurements.....	35
4.1.2. Optical Emission Spectroscopy measurements.....	37
4.1.2.1. Measurements of electron temperature and electron density .....	42
4.2. Responsivity of the GDD.....	46
4.3 MM-wave imaging using GDD as a single pixel detector.....	51
5. CONCLUSION .....	53
REFERENCES.....	55

## LIST OF TABLES

### TABLES

Table 2.1 Ionization and metastable energies of inert gases. Data is taken from NIST. .....	6
Table 4.1 Spectroscopic details of observed xenon and neon lines. The data is taken from the NIST database. ....	38

## LIST OF FIGURES

### FIGURES

Figure 2.1 The typical schematics of low pressure dc glow discharge between electrodes.....	3
Figure 2.2 Multiplication of electrons in an electric field. Figure is adapted from [15] .....	7
Figure 2.3 The voltage-current characteristics curve for low pressure plasma [10].	10
Figure 2.4 Spatial distribution of dark and bright regions, electric field E, electron and ion charge densities [10]. .....	12
Figure 2.5 Example of Boltzman plot used to determine electron temperature [21].	15
Figure 2.6 Ac equivalent circuit for plasma. ....	22
Figure 3.1 Physical dimensions of Glow Discharge Detectors. ....	25
Figure 3.2 Schematics of the electrical circuit used to generate and analyze the dc glow discharge.....	26
Figure 3.3 Photograph and schematic diagram of the experimental setup for examining the emission spectrum. ....	27
Figure 3.4 Schematics of the experimental setup for studying GDD detection dependence on the discharge current and the frequency of the incident radiation. L1 is the TPX lens (50 mm diameter, F#3) and L2 is the teflon lens (50 mm diameter, F#2). .....	29

Figure 3.5 Photograph of the experimental setup demonstrated to study GDD-mm-wave interactions.....	29
Figure 3.6 Schematics of the amplifier circuit for detection purposes. ....	30
Figure 3.7 The response of the designed amplifier circuit as a function of frequency. The gain of the circuit is found as 38.2 dB at frequency about 700 Hz.....	31
Figure 3.8 The response of the designed amplifier circuit as a function of frequency. The gain of the circuit is found as 37.7 dB at frequency about 700 Hz.....	31
Figure 3.9 Front panel of the LabVIEW code used to control motorized stage and collect data. ....	32
Figure 3.10 Photograph of the 24X24 pixel “F” shaped object. ....	33
Figure 3.11 Schematics of the raster scan mm-wave imaging system. L1 is the TPX lens (50 mm diameter, F#3). L2, L3 and L4 are teflon lens (50 mm diameter, F#2). 34	34
Figure 3.12 Photograph of the experimental setup for imaging applications. ....	34
Figure 4.1 Measured DC voltage between the electrodes of N520 A as a function of the discharge current. ....	36
Figure 4.2 Measured DC voltage between the electrodes of N523 as a function of the discharge current. ....	36
Figure 4.3 The resistance of the generated dc glow discharge inside a) N523 and b) N520A as a function of the discharge current.....	37
Figure 4.4 Experimental emission spectrum of N520A recorded in the spectral region from 580 nm to 730 nm at 9 mA. The line intensity profile is obtained by using LEOI-100 CCD spectrometer. ....	40

Figure 4.5. Experimental emission spectrum of N523 recorded in the spectral region from 580 nm to 730 nm at 9 mA. The line intensity profile is obtained by using LEOI-100 CCD spectrometer. .... 40

Figure 4.6 Experimental emission spectrum of N523 recorded in the spectral region from 500 nm to 1000 nm at 9 mA. The line intensity profile is obtained by using StellarNet spectrometer. .... 41

Figure 4.7 Intensity of three neon lines as a function of discharge current for a) N520A and b) N 523. .... 42

Figure 4.8 Boltzmann plot to calculate the electron temperature of the dc glow discharge plasma inside N 520A at 9 mA. .... 43

Figure 4.9 Boltzmann plot to calculate the electron temperature of the dc glow discharge plasma inside N 523 at 9 mA. .... 43

Figure 4.10 The stark broadened profile of the Ne I line at 585.25 nm for N520A discharge lamp. The red line is the Voigt fit of the experimentally observed profile. .... 45

Figure 4.11 The stark broadened profile of the Ne I line at 585.25 nm for N523 discharge lamp. The red line is the Voigt fit of the experimentally observed profile. .... 45

Figure 4.12 Blue line is the detected signal by GDD and red line is the TTL modulation signal given by function generator to modulate mm-wave source. Modulation frequency is 700 Hz. .... 46

Figure 4.13 Responsivity of N523 as a function of the current at two different radiation frequencies. .... 48

Figure 4.14 Responsivity of N520A as a function of current at two different radiation frequencies. .... 48

Figure 4.15 Normalized signal for a N523 discharge lamp with varying rotation angle. .....	49
Figure 4.16 The waveform of the detected signal at 87 GHz and GDD operates at 6 mA discharge current. ....	50
Figure 4.17 24x24 pixel mm-wave images of the “F” shaped object obtained by the N523 GDD at the 87 GHz radiation frequency.....	51
Figure 4.18 24x24 pixel mm-wave images of the “F” shaped object obtained by the N523 GDD at the 100 GHz radiation frequency.....	52
Figure 4.19 24x24 pixel mm-wave images of the “F” shaped object obtained by the N523 GDD at the 119 GHz radiation frequency.....	52

## LIST OF ABBREVIATIONS

CW	Continuous wave
FWHM	Full width half maximum
He-Ne	Helium neon
THz	Terahertz
GDD	Glow Discharge Detector
DC	Direct Current
NIST	National Institute of Standards and Technology
Ne	Neon
Ar	Argon
Xe	Xenon
OES	Optical Emission Spectroscopy
Hz	Hertz
GHz	Gigahertz
nm	nanometer
2D	Two dimensional
1D	One dimensional
EM	Electromagnetic
AC	Alternative Current

## CHAPTER 1

### INTRODUCTION

Millimeter wave region of the electromagnetic spectrum, corresponding to 30–300 GHz band, has a variety of different applications in several fields due to its unique characteristics. Higher frequency of the band translate to higher data transfer rates, making mm-wave a suitable choice for wireless and satellite to satellite communication [1-3]. Additionally, millimeter wave have applications in medicine and biology, since it is strongly absorbed in water and media including biological structures. Millimeter waves have energies in the range of meV. Due to their low photon energy property, they do not initiate chemical reaction which results in damaging DNA or tissue molecules. Since millimeter waves cannot penetrate entire body, they mostly used in monitoring in skin, breast, mouth cancers [4]. Besides the fields of medicine and communication, millimeter waves have various applications in non-destructive testing. There are several methods for inspection of flaws in materials such as X-ray and ultrasonic waves. However, the contrast between flawless and defective surfaces cannot be well distinguished using the X-ray method. Reference [5] gives an example in which they designed a detector to detect millimeter waves radiating from the fruits. By this way, they can conclude whether fruit is ripe or not. Moreover, millimeter waves can penetrate a wide variety of non-metallic and non-polar materials. This property alone allows detection of illicit substances and weapons through clothing and other obstacles such as soil and walls. The capability to detect mentioned devices is crucial in defeating terrorism. Millimeter standoff systems have been developed for security applications [6]. There are two modes of millimeter wave imaging systems: active and passive imaging systems.

The object radiate electromagnetic radiation depending on its temperature. In the case of passive imaging, the contrast between background radiation and radiation due to object is recorded [7].

The active imaging systems are most commonly used in the millimeter band. In this case, the target is illuminated using a millimeter-wave source, then reflected or transmitted radiation is measured using a detector. The frequency and power of the radiation can be selected depending on the application type. The positions of detector and radiation source is very crucial to obtain good results. The Continuous Wave (CW) imaging is one of the main method in active imaging. The design of the CW active imaging system depends of the application. In the CW imaging method, the amplitude of the reflected or transmitted signal is measured using a detector. The frequency domain, time domain and depth information cannot be obtained in CW method. In this thesis, the CW active imaging system is constructed and detailed information is given in Chapter 3 [8].

Detectors are the most important components of the imaging systems. Researchers tend to search new technologies to reduce the cost of systems. The uncooled detectors should be employed in imaging systems to make them cost-effective. In the case of cooled detectors, cooling improves sensitivity of them. There is a lack of commercially available uncooled room temperature detectors in mm-wave and THz regions. There are several type of room temperature detectors such as Golay Cells, Schottky barrier diodes, microbolometers, pyroelectric detectors. Depending on the application, each of the mentioned detectors can be advantageous [9].

In this study, two type of miniature indicator lamps (GDDs) are commercially obtained (International Light Technologies, Peabody, MA, USA) and characterized. The plasma parameters of these discharge is investigated by Optical Emission Spectroscopy. The relation between discharge current and discharge voltage is studied to determine the working mode of the glow discharge. Furthermore, these discharge lamps are employed as millimeter wave detectors. The responsivity of these detectors are tested for different discharge current values and polarization angles. Finally, these detectors are used as a single pixel detector in a raster scan millimeter wave imaging system.

## CHAPTER 2

### THEORETICAL BACKGROUND

#### 2.1. DC Glow discharge

There exists many different types of glow discharges depending on the application. The gas component, the pressure inside chamber and the dimension of the chamber affect the type of the glow discharge. The material, size of electrodes and distance between electrodes also has an effect on the glow discharge type.

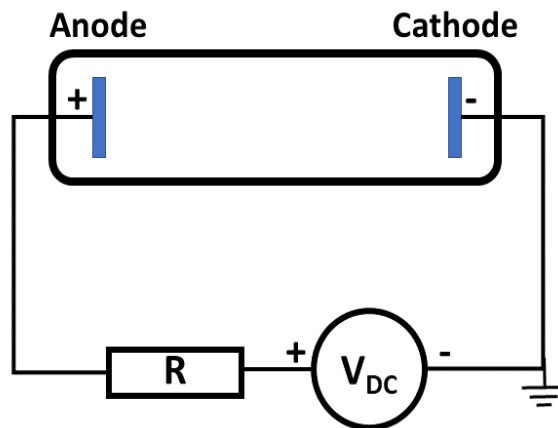


Figure 2.1: The typical schematics of low pressure dc glow discharge between electrodes.

In our case, we focus on the glow discharge driven by a dc power supply. The dc glow discharge can be obtained by applying a dc potential between the metal electrodes placed in gas. The typical schematics of the electrical circuit for generating dc discharge is shown in Figure 2.1. The resistance is connected in series with the dc power supply and the discharge. The aim of connecting resistance is to limit the current

through the discharge. In order to understand the dc glow discharge, we need to have information on the fundamental process in the discharge.

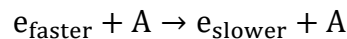
The electric field is generated between the electrodes and it has direction from anode to cathode. The direction of the motion of the charged particles depend on the direction of the electric field. Since the charged particles are in motion, they collide with other charged particles and neutral atoms. The direction of the moving particle changes after each collision and then again accelerated in the parallel direction of the electric field. The motion of the charged particle along the direction between collisions with other particles is known as drift. The drift velocity of a charged particle is given as,

$$\vec{v}_d = \pm \mu_i \vec{E} \quad (2.1)$$

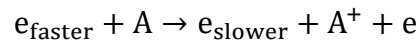
where the  $\pm$  sign can be expressed positive for ions, negative for electrons ,  $\mu_i$  the mobility of particle  $i$  and  $\vec{E}$  is the electric field. The relation between the drift velocity and the electric field is not linear, since the mobility also depends on the strength of the electric field. It is clear that electrons move toward the anode, however, the ions tend to move toward the cathode. The drift velocity for the electrons is higher than the ions' drift velocity, since electrons are much lighter than ions [10].

### 2.1.1. Collisions in gas discharge

In weakly ionized discharge, the contribution of electrons is higher than the ions and most collisions are dominated by electrons. Moving electrons participate in elastic and inelastic collisions with other particles. In an elastic collision case, a moving electron collides with a neutral particle and changes its direction without significant change in its speed. The energy transferred from the electron to the neutral particle during their collision equals to  $4m_e m_n / (m_e + m_n)^2$  fraction of the initial energy of the electron. Since the neutral atom (A) is heavier than the electron, the transferred energy is ignorable. The speed of the scattered electron slightly decreases after collision, e.g.

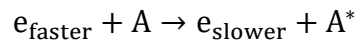


The inelastic collision, however, has an important role in generating and sustaining glow discharge. The ionization and excitation processes are related to the inelastic collisions of electron with other particles. During an inelastic collision, if the electron has sufficient enough energy, it may remove bounded electrons from an atom. This required energy is called the ionization potential. Two electrons and positive ion ( $A^+$ ) are obtained at the end of this ionization process, e.g.



The produced electrons again accelerated due to electric field toward the anode. They gain energy from the electric field and participate in similar inelastic collisions which lead to production of new electrons. This fundamental process also known as the electron impact ionization.

Contrast to the ionization process, in the excitation process new electron is not produced after an inelastic collision. In this case, bound electron jumps to a higher energy level in the atom due to transferred energy after collision. The minimum energy required for the process is called as the excitation potential. At the end of an excitation process, the moving electron gives its certain energy to the neutral atom, it slows down.



The excited atom is represented as  $A^*$ . The ionization potential is higher than the excitation potential of the atom. For example, for neon the excitation potential is 16.6 eV and ionization potential is 21.6 eV according to the NIST [11]. Both processes occur in the weakly ionized discharge and contribute to the glow discharge.

Metastable atoms are excited atoms which do not radiate very long time. The ionization and metastable energies of inert gases are listed in Table 2.1. It can be seen that metastable energy of inert gases is lower than the ionization energy of them. Consider two different inert gases inside a tube. If the energy of the metastable atom ( $A^*$ ) is higher than the ionization energy of the neutral atom, the collision among them will lead to ionization of the neutral atom. This effect is known as the Penning ionization.



For example, consider Ne-Ar penning mixture. The metastable energy of the Ne is 16.6 eV and the ionization energy of the Ar is 15.8 eV. The energy difference between them is about 0.8 eV. Thus, the neon in the metastable state can ionize the argon and it will trigger the discharge [12].

Table 2.1: Ionization and metastable energies of inert gases. Data is taken from NIST.

Inert Gas	Ionization Energy (eV)	Metastable Energy (eV)
Helium	24.6	19,8
Neon	21.6	16.6
Argon	15.8	11.6
Xenon	12.1	8.3

### 2.1.2. Electron emission from the electrode

Electron emission from the surface of the cathode is an important mechanism to sustain dc glow discharge. A certain amount of energy is required extract electron from the surface of cathode. This required energy is called the work function. The work function has a different values for different materials [13]. The materials with lower work function is generally preferred for the electrodes. The lower work function means lower energy required to extract an electron.

There are several mechanisms that result from the extraction of an electron from the surface of the electrode. The most pronounced mechanism is the secondary electron emission which can be observed at the anode and at the cathode. In this case, particles such (electrons, ions, neutrals, metastable atoms and photons) with a sufficient energy collide with a surface and an electron is released from the surface. The number of electrons extracted per incident particle is known as secondary electron coefficient and represented by the coefficient  $\gamma$ . The secondary electron coefficient depends on the type and the energy of the incident particle.

The electron can be released due to electron bombardment of the surface. Since the sign of the cathode is negative, the electron cannot move towards it. Thus, no

electron bombardment can be observed at the cathode. Most of the electrons strike the anode. The electron can also be extracted from the surface by ion and neutral atom bombardment. The secondary electron is obtained by Auger process. Moreover, the secondary electron can be obtained as a result of photon bombardment and also known as photoemission. In this case, the energy of the photon must be higher than the work function of the surface material [14].

### 2.1.3. Townsend Breakdown Process

Breakdown theory of the low pressure glow discharge is explained by J.S. Townsend. Suppose that a dc voltage is applied to electrodes and strong electric field is generated. The distance between anode and cathode is  $d$ .

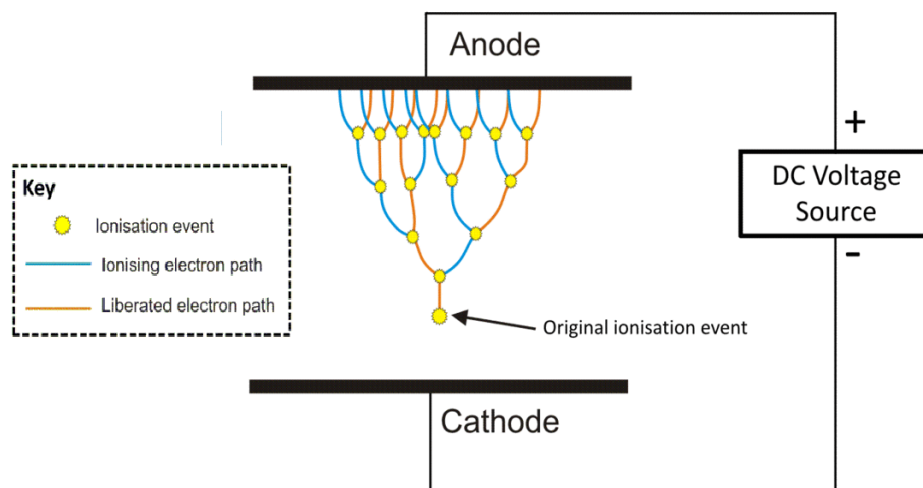


Figure 2.2: Multiplication of electrons in an electric field. Figure is adapted from [15]

Irradiating cathode with UV light cause electron emissions from the surface by the photoionization process. Breakdown process begins with a free electron emitted from the surface of the cathode. The electron is accelerated toward the anode by the electric field. The accelerated electron collides with a neutral atom on its way and ionize the neutral atom by the electron impact ionization process. After first ionization process, there are two electrons and one ion presented in the discharge environment. These electrons also gain sufficient energy by the electric field and ionize two more neutral

atoms. We have four electrons and three ions at the end of the second ionization process. As the electrons drift toward the anode, they ionize neutral atoms on their way and the electron avalanche evolve in time. The ionization process is visualized in Figure 2.2. The number of electrons generated in an electron avalanche can be expressed as,

$$N_e(x) = N_0 e^{\alpha x} \quad (2.2)$$

where  $\alpha$  is the ionization coefficient,  $N_0$  is the number of electrons produced by irradiation of cathode in per second and  $x$  is the distance from the cathode. The value of the ionization coefficient depends on the electric field, type and pressure of the gas. The accelerated electrons ionize neutral atoms and as a result ions are produced. The number of ions ( $N_i$ ) produced in electron avalanche can be expressed as,

$$N_i(x) = N_0(e^{\alpha x} - 1) \quad (2.3)$$

The produced ions move toward the cathode. As explained before, the number of ions is one less than number electrons in the medium. Up to now we only consider the effect of electron impact ionization in the breakdown process. However, this ionization process is not enough to generate and sustain the glow discharge. The ions hitting the cathode surface result in new electrons called the secondary electrons. The number of secondary electrons can be written as,

$$N_{\text{sec,e}}(d) = \gamma N_0(e^{\alpha d} - 1) \quad (2.4)$$

where  $N_{\text{sec,e}}$  is the number of electrons produced as a result of the secondary emission process,  $\gamma$  is the secondary emission coefficient. These secondary electrons are accelerated by the electric field. These accelerated electrons make collisions with other neutral atoms in medium, as a result new ions and electrons are produced. It can be concluded that both the electron impact ionization and the secondary emission process have a significant roles in the breakdown and sustaining glow discharge. All electrons reached the anode in this multiplication process giving by,

$$N_{\text{e at anode}} = N_0 \left[ e^{\alpha d} + \gamma(e^{\alpha d} - 1)e^{\alpha d} + \gamma^2(e^{\alpha d} - 1)^2 e^{\alpha d} + \dots \right] \quad (2.5)$$

After simplification of the above equation the total current through circuit can be found as,

$$\frac{I}{I_0} = \frac{N_e}{N_0} = \frac{e^{\alpha d}}{1 - \gamma(e^{\alpha d} - 1)} \quad (2.6)$$

where  $I_0$  is the initial current due to UV light irradiation.

The current through the circuit due to the secondary emission and the electron impact ionization process is given by the equation 2.6. If the denominator of this equation is positive, i.e.,  $1 > \gamma(e^{\alpha d} - 1)$ , the discharge is not a self-sustained type. Due to positive denominator, the current decreases over time if there is no external is present to trigger ionization processes.

If  $\gamma(e^{\alpha d} - 1) \geq 1$ , the increase in the applied voltage causes further electron impact ionization and the secondary emission over time. Theoretically, the current goes to infinity, however, an external resistance limits this in practice. This type of discharge does not depend on the external source to trigger ionization, then it is self-sustained [10].

#### 2.1.4. Current-Voltage (I-V) Characteristics

The behavior of the potential across the electrodes depends on the value of the current through the circuit shown in Figure 2.1. The current flowing through the circuit is controlled by a dc power supply and an external resistance. The current-voltage characteristics of a low pressure discharge is presented in Figure 2.3. As can be seen from I-V characteristics curve, the discharge has different modes depending on the current. The voltage between the electrodes of the discharge can be expressed as,

$$V = \mathcal{E} - IR, \quad (2.7)$$

where  $\mathcal{E}$  is the applied voltage by the power supply,  $R$  is the resistance of the external resistor and  $I$  is the current through circuit. This equation is known as the load line. The current through discharge can be manipulated by changing either the resistance or the voltage applied by power supply.

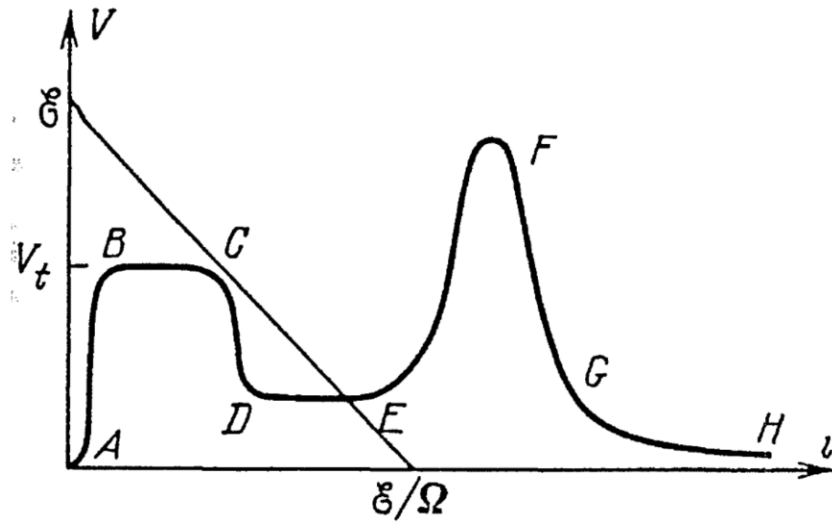


Figure 2.3: The voltage-current characteristics curve for low pressure plasma [10].

If the applied voltage between electrodes is very low and the value of the resistance is high, an extremely weak current can be observed. In this region, electrons generated by a low potential and external sources (cosmic rays or UV rays) cause low current flowing through the circuit. The energy of the electrons is not sufficient to ionize neutral atoms due to a very low potential across electrodes in the region between A and B. The applied voltage should be increased to increase the current through discharge. The electron multiplication is not enough to sustain the discharge until an exact potential value is obtained. The discharge type in the region between B and C is called the Townsend dark discharge. In the case of the Townsend discharge mode, I-V curve is nearly flat since the electron and ion densities are negligible.

The transition from a non-self-sustaining mode to self-sustaining mode is achieved when the potential across electrodes is reached to a sufficiently high potential, known as the breakdown voltage. The current can be increased whether by increasing the voltage of the power supply or by reducing the value of the load resistor in equation 7. The glow discharge mode begins just after the breakdown occurs. The glow discharge mode can be obtained directly by applying a voltage greater than the breakdown voltage. In this case, electrons accelerate due to high electric field and produce new electrons. Also secondary electrons are generated by the ions. The D-E part of the I-V curve corresponds to a normal glow discharge where the cathode is

covered by the glow. The color of the glow depends on the gas used in the discharge. As it can be seen from Figure 2.3, the voltage on the discharge remains the same while the current is increasing. The glow covered cathode expands proportionally with the increase in current and thus the current density at the cathode remains constant in the normal glow mode. The normal glow mode ends when the whole cathode is covered by glow completely. The current density begins to increase with increasing current in the abnormal glow mode which is observed between points E and F. The increase in the current leads to a sharp rise in the voltage across the discharge presented in Figure 2.3. Both in normal and abnormal modes, most of the atoms are ionized [10].

### **2.1.5. Layers of the gas discharge**

The bright luminous and dark layers are arranged between the cathode and anode as shown in Figure 2.4. The appearance of the glow discharge depends on the pressure and the type of the gas, material and the separation of the electrodes, the current through the discharge. Distribution of the electric field gives an idea about the axial motion of the electrons and the positive ions. The electric field has its maximum value near the cathode and begins to decrease gradually until Faraday darks space. The electric field is nearly constant at the positive column. The first layer close to the cathode is called the Aston dark space which occupies a very narrow space. The electrons which are ejected from the cathode have a very low energy less than 1 eV forming the Aston dark space. The electric field strength is at a maximum near the cathode. The electrons gain energy by the electric field and accelerate toward the next region which is known as the cathode glow. The electrons participate in inelastic collisions in which they excite neutral atoms. As a result of the excitation process, glow is occurred. Ions density is high in cathode glow region. The cathode dark space begins just after the cathode glow region. The electron energy increases with an increase in distance from the cathode, and decreases after the cathode layer with increasing distance from the cathode. Since the energy of electrons in the cathode dark space is very high, they participate in the ionization processes. Most ionizations of neutral atoms take place in this region. New electrons generated at the end of cathode

the layer, thus the electron density is very high at the boundary of the negative glow and the cathode dark space.

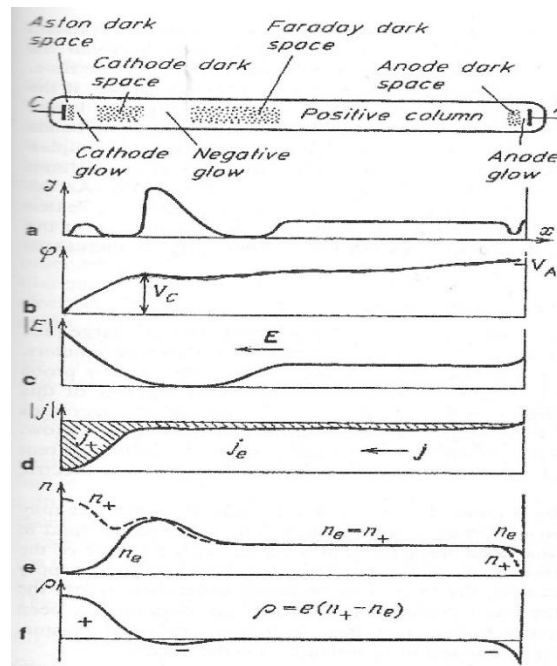


Figure 2.4: Spatial distribution of dark and bright regions, electric field  $E$ , electron and ion charge densities [10].

After the cathode dark space, the most luminous part of the discharge begins, which is known as the negative glow region. Brightness of the region reduces toward the anode. The electrons generated at the cathode dark space enter the negative glow region. The energy of these electrons is not enough to ionize neutral atoms. However, they have sufficient energy to excite atoms and glow is occurred. Since they participated in only few collisions, they have sufficient energy to ionize neutral atoms. Electrons which participated in the excitation and the ionization processes lose most of their energy and Faraday dark space is formed. The electric field slightly increases in the Faraday dark space. As a result electrons are accelerated by the field and participate in excitation process in the positive column region [10]. The brightness of the negative glow is higher than that of the positive column. The electric field remains constant in positive column. The color of the glow depends on the type of the gas. For neon gas, colors of the negative glow region and positive column are orange and brick red, respectively [16].

When the pressure inside the glow tube is increased, the layers of the discharge turn into thinner and move towards the cathode. The reverse effect can be observed when the pressure is decreased. The distance between the anode and the cathode has an effect on layers of discharge. If the anode is moved toward the cathode, the positive column becomes thinner. The positive column is disappeared when the inter-electrode space is very short, whereas, the axial length of the negative zones are not affected [17].

## 2.2. Optical Emission Spectroscopy

The Optical Emission Spectroscopy (OES) is one of the most widely used technique to study plasma parameters such as electron temperature and electron density. In OES method, the intensity of light emitted from a plasma is recorded as a function of wavelength. During the measurement, the plasma is not disturbed and being non-invasive is the main advantage of OES method. As briefly explained in the previous sections, electrons make inelastic collisions to excite neutral atoms. In this case, the state of atom rises to a higher electronic state. The bound electron in an excited state undergoes a transition from a higher state to a lower state, then a photon is emitted in a specific wavelength. The energy of the emitted photon can be written as,

$$E_p - E_q = \frac{hc}{\lambda_{pq}} \quad (2.8)$$

where  $\lambda_{pq}$  is the wavelength,  $h$  is the Planck's constant,  $E_p$  is the energy of the upper state and  $E_q$  is the energy of the lower state [18]. The intensity of the spectral line which results from the transition of the atom from p state to q state, in the case of LTE conditions, is given by [19],

$$I_{pq} = \frac{hcA_{pq}g_p n}{\lambda_{pq}U(T)} \exp(-E_p/k_B T) \quad (2.9)$$

where  $A_{pq}$  is the transition probability between states p and q,  $g_p$  is the statistical weight of the upper energy state, n is the number density of the emitting species,  $U(T)$  is the partition function of atom,  $E_p$  is the energy of the upper state,  $k_B$  is the Boltzmann's constant and T is the excitation temperature. The spectroscopic data can be obtained from the NIST database.

### 2.2.1. Measurements of the electron temperature

The electron temperature is an important characteristics of the plasma and can be estimated by using OES. It can be found in several ways. In the LTE conditions, the electron temperature is equal to the excitation temperature mentioned in equation 2.9. The electron temperature can be found directly using equation 2.9, as long as, the plasma satisfies the LTE condition.

#### 2.2.1.1. The line ratio method

The electron temperature can be determined using ratio of the intensity of the spectral lines belonging to the same atomic species. In this method, two different spectral lines are chosen from the emission spectrum. The intensities of spectral lines which are obtained as a result of transition from  $p \rightarrow q$  and  $m \rightarrow n$  are denoted as  $I_{pq}$  and  $I_{mn}$ , respectively. By using the equation 2.9, the intensity ratio of two spectral lines of same species can be written as,

$$\frac{I_{pq}}{I_{mn}} = \frac{\lambda_{mn} g_p A_{pq}}{\lambda_{pq} g_m A_{mn}} \exp\left(-\frac{E_p - E_m}{k_B T_e}\right) \quad (2.10)$$

The electron temperature can be deduced from equation 2.10. The accuracy of this method is limited, if the difference between  $E_p$  and  $E_m$  is small. The sensitivity of the equation 2.10 can be improved, if the upper energy levels of two selected lines have larger difference [20].

### 2.2.1.2. The Boltzmann Plot method

In previous case, the electron temperature is determined using only two spectral lines. In order to reduce error, more spectral lines should be involved in determination of the electron temperature. The Boltzmann plot method is widely used to determine the electron temperature. Several spectral lines belong to same species are used in this method. The equation 2.9 is rearranged and written in new form as follows,

$$\ln \left[ \frac{I_{pq} \lambda_{pq}}{A_{pq} g_p} \right] = - \frac{1}{k_B T_e} E_p + \ln \left[ \frac{n}{U(T)} \right] \quad (2.11)$$

Plotting above equation gives linear relationship which has a slope of  $-1/k_B T_e$  as shown in Figure 2.5. The slope is sensitive to the intensity of the spectral line. The uncertainty in measurement of intensity will affect the accuracy of the electron temperature measurement. The electron temperature is deduced from the slope of plot. Finding the best fitting straight line improves the accuracy of the Boltzmann plot method. The spectral lines with the largest difference between their upper energy levels are selected to make the plot more meaningful [21].

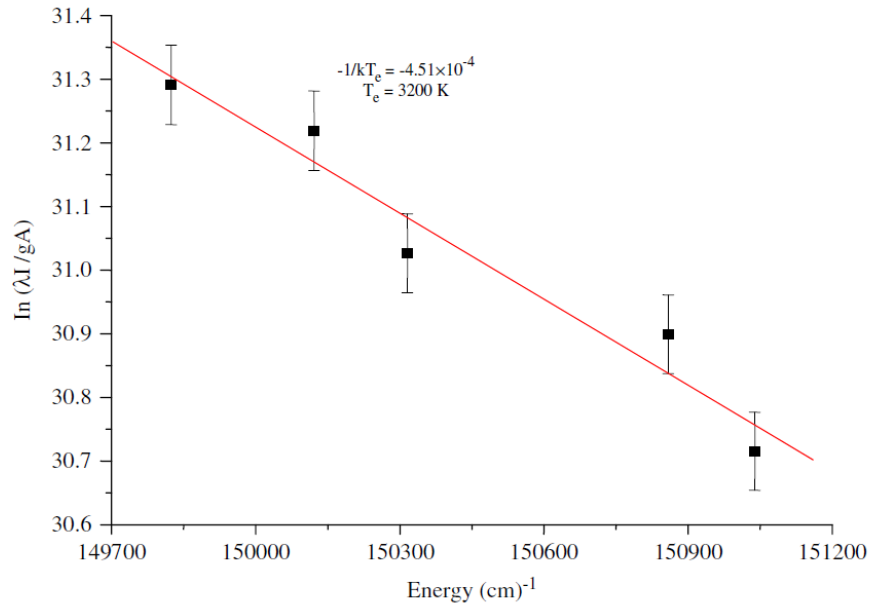


Figure 2.5: Example of Boltzman plot used to determine electron temperature [21].

### 2.2.2. Measurements of the electron density

The electron density is another important parameter to characterize the plasma. In an optical emission spectrum, the lines can be broadened and shifted due to Stark, Doppler, natural and instrumental broadening [22]. As a result of collisions of emitting atoms with electrons and atoms, the spectral line is broadened and this effect is known as the Stark effect. The Stark broadening method is a widely used method to determine the electron density. The line profile of the Stark broadening is well suited to the Lorentzian form and has a full width half maximum (FWHM) which is related to the electron density. The FWHM of the broadened line, due to Stark effect is given by [23],

$$\Delta\lambda_{1/2} = 2w \left( \frac{n_e}{10^{16}} \right) + 3.5A \left( \frac{n_e}{10^{16}} \right)^{\frac{1}{4}} \left( 1 - \frac{3}{4} N_D^{-\frac{1}{3}} \right) w \left( \frac{n_e}{10^{16}} \right) \quad (2.12)$$

where  $n_e$  is the electron density,  $w$  is the electron impact parameter,  $N_D$  is the number of particles in a Debye sphere and  $A$  is the ion broadening parameter. The contribution of ion collisions to the broadening is negligible. So the second part of the equation 2.12 vanishes. The FWHM of spectral line is reduced to

$$\Delta\lambda_{1/2} = 2w \left( \frac{n_e}{10^{16}} \right) \quad (2.13)$$

Before calculating the electron density using the above equation, it is required to optimize FWHM of the spectral line. The real FWHM of spectral line can be found by subtracting the observed FWHM from the instrumental broadening.

$$\Delta\lambda_{\frac{1}{2}(real)} = \Delta\lambda_{observed} - \Delta\lambda_{instrument} \quad (2.14)$$

The real broadening of the spectral line is a convolution of Gaussian and Lorentzian profiles, which is known as Voigt profile. The FWHM of the Voigt profile is used for determining Stark broadening of the spectral line.

### 2.3. GDD-Millimeter Wave Interaction

For a weakly ionized plasma, the equation of 1D motion for a charged particle in the discharge in the presence of an electric field  $\vec{E}$  can be described as [24-25],

$$m \frac{d\vec{v}}{dt} + \nu m \vec{v} = q \vec{E} \quad (2.15)$$

where  $m$ ,  $\vec{v}$  and  $q$  are the charged particle's mass, velocity and electric charge, respectively,  $\nu$  is the electron neutral collision frequency. Since the velocity of the electron is much higher than the ion's velocity in any discharge, the primary charged particle in the discharge process is electron. The " $\nu m \vec{v}$ " term in equation describes the effect of the elastic collisions between electrons and neutral atoms. The velocity of the electron decreases after elastic collision, so the mentioned term acts as a frictional force.

Detection of millimeter waves by GDDs can be explained by the electromagnetic wave-plasma interactions. The electromagnetic radiation illuminates the discharge in which there are plenty of free electrons. The electromagnetic radiation heats the free electrons and cause an increase in the kinetic energy of electrons. These accelerated electrons begin to participate in inelastic collisions which lead to generation of new electrons. The newly generated electrons also ionize atoms, if they have sufficient energy. Due to these electrons generated continuously, the discharge current will increase. The process is known as the enhanced cascade ionization which mostly takes place at the end of the cathode dark space where the total electron energy is high. When the discharge operates in normal and abnormal modes, most of atoms can be found in an excited and/or ionized state. In such case, the enhanced cascade ionization can be obtained easily, since atoms need small energy to ionize. Moreover, EM wave can also contribute to the ionization process. Contrast to the enhanced cascade ionization, some of charged particles may gain energy from the incident electromagnetic wave move toward the walls of the tube, resulting a diffusion process causing a decrease in the discharge current. The change in the discharge current as a result of the enhanced cascade ionization and the diffusion process is given as [26],

$$\Delta I_d = (\Delta v_i)n + v_i(\Delta n) - (\Delta D)\nabla^2 n - D\nabla^2(\Delta n) \quad (2.16)$$

where  $v_i$  is the ionization collision frequency,  $n$  is the electron density and  $D$  is the diffusion coefficient. The effect of the diffusion phenomenon mostly pronounced in the Faraday dark space region where the electron energy is very low [26].

In order to study the enhanced cascade ionization, the equation 2.15 is modified. Since the random velocity of free electron changes after the energy gain from the EM radiation, the modified equation of motion of the electron can be expressed as,

$$m \frac{d(\Delta \vec{v})}{dt} + vm\Delta \vec{v} = q\vec{E} \quad (2.17)$$

where  $\Delta \vec{v}$  is the change in the random electron velocity due to the incident EM radiation and  $\vec{E}$  is the electric field of the incident EM wave. If the electric field of the EM wave is considered in the x-direction, the change in the velocity must be in the same direction with the electric field. The electric field of the EM wave and change in the velocity can be written as,

$$\vec{E}_x = E_0 e^{j\omega t} \hat{i} \quad (2.18)$$

$$\Delta \vec{v}_x = \Delta v_0 e^{j\omega t} \hat{i} \quad (2.19)$$

where  $\omega$  is the angular frequency of the EM wave. Substituting  $\Delta \vec{v}$  and  $\vec{E}_x$  in the equation 2.17, the change in the velocity in the x-direction can be found as,

$$\Delta \vec{v}_x = \frac{q}{m(\nu + j\omega)} \vec{E}_x \quad (2.20)$$

The change in the current density can be expressed as,

$$\Delta \vec{J}_x = nq\Delta \vec{v}_x = \frac{nq^2}{m(\nu + j\omega)} \vec{E}_x \quad (2.21)$$

The kinetic energy gain by the EM wave is equal to the work done by the field of the EM wave on the charged particle. The rate of gain of the kinetic energy by the EM wave can be found by Poynting's Theorem.

$$\int_V (\vec{E} \cdot \vec{J}) dV = - \oint_S (\vec{E} \times \vec{H}) dS - \frac{1}{2} \frac{d}{dt} \int_V (\epsilon \vec{E}^2 + \mu H^2) dV \quad (2.22)$$

The first term of the right-hand-side is the energy flowing out through the boundary surfaces per unit time, the second term of the right-hand-side is the change in the energy stored in both the electric and the magnetic field. The term on the left-hand-side is the rate of change of energy of all particles contained in the volume V [27-28]. Thus the time averaged rate of change of kinetic energy gain of the electron due to the incident EM wave per volume can be written as,

$$\frac{du}{dt} = \frac{1}{2} [\vec{E} \cdot \vec{J}] = \frac{nq^2 E_x^2}{2m(\nu + j\omega)} \quad (2.23)$$

In order to find the averaged power density of the incident EM wave, the first term the of RHS of the equation 2.22 is used.

$$P_D = \frac{1}{2} \frac{E_x^2}{\eta_p} \quad (2.24)$$

where  $\eta_p = \sqrt{\mu_p/\epsilon_p}$  is the plasma wave impedance which is a function of the plasma permittivity  $\epsilon_p$  and permeability  $\mu_p$ . The plasma permittivity is [29]

$$\epsilon_p(\omega) = \epsilon_0 \left\{ 1 - \frac{\omega_p^2}{\omega^2 + \nu^2} - j \frac{\omega_p^2 \nu}{\omega(\omega^2 + \nu^2)} \right\} \quad (2.25)$$

where  $\omega_p = \sqrt{nq^2/m\epsilon_0}$  is the plasma frequency. The transmission of incident radiation through the plasma depends on the plasma frequency. The transmission of incident radiation increases with increasing EM wave frequency for identical plasma density [30-31]. Then the plasma wave impedance for  $\omega \gg \omega_p$ , since the plasma frequency is about a few GHz for a weakly ionized plasma, can be obtained as,

$$\eta_p = \sqrt{\frac{\mu_p}{\epsilon_p}} = \eta_0 \sqrt{\frac{\epsilon_0}{\epsilon_p}} = \eta_0 \left\{ 1 + \frac{\omega_p^2(\omega + j\nu)}{2\omega(\omega^2 + \nu^2)} \right\} \quad (2.26)$$

By substituting the equation 2.24 and 2.26 into the equation 2.23, the time averaged rate of change of kinetic energy gain of electron due to the incident EM wave per volume for  $w \gg w_p$  is found as [32],

$$\frac{du}{dt} = \frac{w_p^2 \nu P_D}{c(w^2 + \nu^2)} \quad (2.27)$$

The change of kinetic energy per unit time is proportional to the electron density, the average power of the EM radiation and the plasma frequency. In the discharge medium, the electrons gained energy from incident EM wave participate in ionization, excitation and elastic collisions. If the gained energy is not sufficient to participate in excitation and ionization collisions, the electrons scatter. The ionization and excitation occur when the energy of the electron is higher than the ionization and the excitation energy of an atom, respectively. The change in the EM wave induced electron energy due to elastic and inelastic collisions as a function time can be written as [32],

$$\Delta\epsilon(t) = \frac{\tau \eta_0 q^2 \nu P_D}{m(w^2 + \nu^2)} (1 - e^{-t/\tau}) \quad (2.28)$$

Since the interaction between the discharge and the incident EM-wave give rise to the discharge current in the enhanced cascade ionization mechanism, the change in discharge current as a function of time is given [32],

$$\Delta I_d = qVnG\Delta\nu_i(t) \quad (2.29)$$

where  $G$  is the internal signal gain,  $\Delta\nu_i$  is the change in the rate of the ionization as a result of the EM-wave.

$$\Delta\nu_i = \frac{\nu_i \epsilon_i \Delta\epsilon}{(\bar{\epsilon})^2} \quad (2.30)$$

where  $\nu_i$  is the ionization collision rate,  $\epsilon_i$  is the ionization energy of atom and  $\bar{\epsilon} = \frac{mv^2}{2}$  is the average electron energy. Substituting the equation 2.28 and 2.30 into the equation 2.29, the change of the discharge current as function of time is found as,

$$\Delta I_d(t) = \frac{GnVq^2 \tau}{\epsilon_i m \tau_i} \eta_0 P_D \left[ \frac{\nu}{\omega^2 + \nu^2} \right] [1 - e^{-t/\tau}] \quad (2.31)$$

The maximum change in the discharge current is obtained when the electron-neutral collision frequency is equal to the frequency of the incident radiation [32-33]. Moreover, the change in the discharge current has linear dependence on the average power of the incident EM-radiation. The change in the discharge current in frequency domain is,

$$\Delta I_d(s) = \left[ \frac{1}{s} - \frac{1}{s + \frac{1}{\tau}} \right] \frac{GnVq^2 \tau}{V_i m \tau_i} \eta_0 P_D \left[ \frac{\nu}{\omega^2 + \nu^2} \right] \quad (2.32)$$

where  $s=j\omega$ .

In the abnormal mode, the effect of diffusion is negligible. The dominant mechanism in detecting millimeter wave radiation is enhanced cascade ionization [34-36].

### 2.3.1. Response time of the Glow Discharge Detector

The change in the discharge current leads to a small change in the discharge voltage. The discharge voltage change in the frequency domain is expressed as,

$$\Delta V_d(s) = Z_{eq}(s) \Delta I_d(s) \quad (2.33)$$

where  $Z_{eq}(s)$  is the equivalent impedance of the circuit shown in Figure 2.6. After the breakdown, the ac equivalent circuit for a GDD is shown in Figure 2.6. The capacitance derives from the charge at electrodes and potential difference between them. The inductance derives from the magnetic flux which is generated by moving charged particles [37]. The load resistance used to limit excess current in the discharge is parallel to the ac equivalent circuit. The resistance (R) can be obtained from the slope of the Current-Voltage characteristic graph. The resistance is real and positive when the discharge operates in the abnormal glow regime.

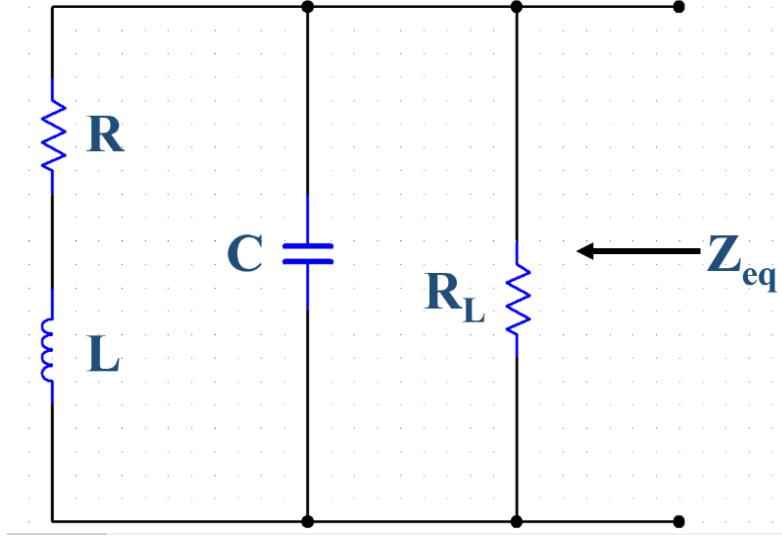


Figure 2.6: Ac equivalent circuit for plasma.

The equivalent impedance of the circuit in the frequency domain is calculated as,

$$Z_{eq}(s) = \frac{1}{C} \frac{s + \frac{R}{L}}{s^2 + 2\alpha s + \omega_0^2} \quad (2.34)$$

where

$$\omega_0^2 = \frac{1}{LC} \left[ 1 + \frac{R}{L} \right] \quad (2.35)$$

$$2\alpha = \frac{R}{L} + \frac{1}{R_L C} \quad (2.36)$$

In abnormal glow mode  $\alpha \approx \omega_0$ , the change in the discharge voltage in frequency domain is

$$\Delta V_d(s) = \frac{1}{C} \frac{s + \frac{R}{L}}{(s + \alpha)^2} \left[ \frac{1}{s} - \frac{1}{s + \frac{1}{\tau}} \right] \frac{GnVq^2}{V_i m} \frac{\tau}{\tau_i} \eta_0 P_D \left[ \frac{v}{\omega^2 + v^2} \right] \quad (2.37)$$

The discharge voltage change in time domain can be obtained by applying the inverse Fourier transform to the equation 2.37 [32],

$$\Delta V_d(t) = \frac{GnVq^2}{\epsilon_i m} \frac{\tau}{\tau_i} \eta_0 P_D \left[ \frac{v}{w^2 + v^2} \right] R_{eq} (1 - e^{-\alpha t}) \quad (2.38)$$

where

$$R_{eq} = \frac{RR_L}{R + R_L} \approx \frac{1}{LC\alpha^2} \quad (2.39)$$

The resistance of the discharge decreases with increasing discharge current, since more ionization process takes place and medium becomes more conductive. The inductance of the discharge also decreases with increasing discharge current. Contrast to the resistance and the inductance, the capacitance increases with increasing in discharge current [37]. In the abnormal mode, the effect of  $\frac{1}{R_L C}$  in the equation 2.36 is very small, since the capacitance increases with increasing discharge current. Then  $\alpha$  is modified as,

$$\alpha = \frac{R}{2L} \quad (2.40)$$

The time required for the output signal to increase from the 10% point to the 90% point of the peak amplitude of the output signal is known as the rise time. The rise time is inversely proportional to term  $\alpha$ . Thus, to decrease the rise time of the detector, it is needed to reduce L in the abnormal glow mode. It can be concluded that the response time of GDD is directly related to the equivalent impedance of the discharge. The rise time can be improved by optimizing electrode separation, pressure and electric field between the electrodes [37].



## CHAPTER 3

### DESCRIPTION OF THE EXPERIMENTAL SETUPS

#### 3.1. Plasma Characterization

##### 3.1.1. Current-Voltage (I-V) Characteristics

The voltage current characteristics of a dc plasma discharge generally depends on the gas type, the gas pressure, the geometry and the material used for the electrodes. The gas pressure inside the GDD lamp is about a few torr. The distance between the anode and the cathode is about 0.4 mm. The nickel electrodes have cylindrical shapes with  $r=0.9$  mm diameter and  $H=3.4$  mm in height. To lower the breakdown voltage, the electrodes of the commercially available discharge lamps are usually coated according to their manufactures.

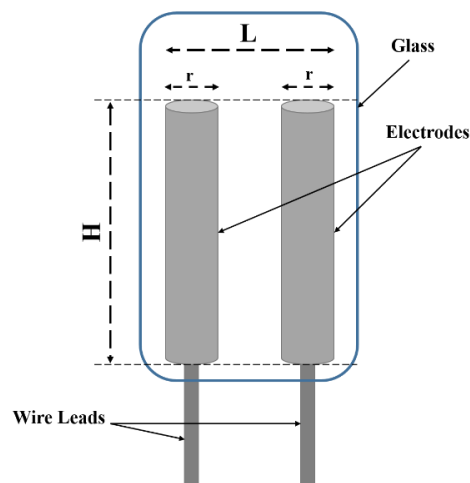


Figure 3.1: Physical dimensions of Glow Discharge Detectors.

Usually barium strontium oxide or barium azide are used for coating since they have high electron emission coefficients. Figure 3.2 is a schematic representation of the electrical circuit used to generate and analyze dc glow discharge plasma. Voltage adjustable dc power supply (Chroma 62012P-600-8), a ballast resistor and a shunt resistor are connected in series to the GDD lamp. The values of the ballast resistor and the shunt resistor are chosen as 5.62 k $\Omega$  and 197.4  $\Omega$ , respectively. The voltmeter is connected to the shunt resistor to monitor the voltage which can be used to calculate current through it. By using this experimental setup, dc voltage on the discharge plasma can be recorded at different current values. The current through the circuit (plasma discharge) is controlled by using the voltage adjustable dc power supply. After the breakdown occurs, the current is recorded by changing the voltage of the dc power supply in 5 V steps. DC voltage on the plasma discharge is computed by using the equation below,

$$V_{\text{GDD}} = V_{\text{DC}} - \frac{V_1}{R_s} (R_s + R_b) \quad (3.1)$$

where  $V_{\text{dc}}$  is the applied voltage by the dc power supply,  $V_1$  is the voltage on the shunt resistor and  $V_{\text{GDD}}$  is the voltage between the electrodes of the plasma discharge.

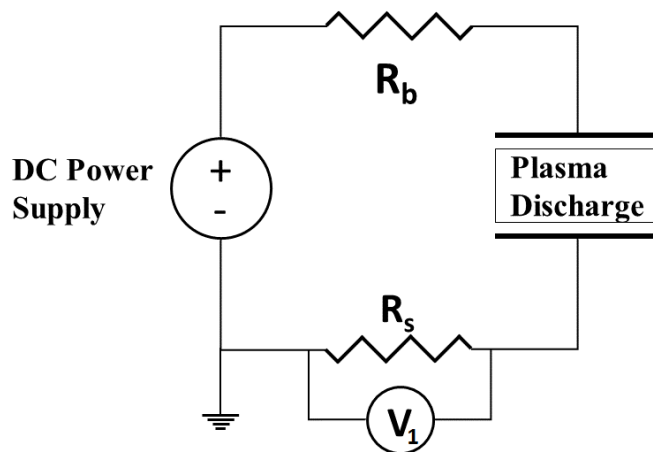


Figure 3.2: Schematics of the electrical circuit used to generate and analyze the dc glow discharge.

### 3.1.2. Optical Emission Spectroscopy

Plasma parameters such as gas species, electron temperature and electron density can be determined using optical emission spectroscopy. Langmuir probe method is also widely used method to determine the parameters of the plasma. Since we cannot put probe inside the GDD lamp, the OES is the best method to study plasma parameters. Figure 3.3 presents photographs of the experimental setups used to determine the plasma parameters of the GDD lamps. LEOI-100 CCD spectrometer (Lambda Scientific Systems, Inc) and StellarNet Inc. spectrometer are employed to examine the emission spectrum of two lamps. LEOI-100 CCD and StellarNet spectrometers cover the spectral region of 300-900 nm and 300-1100 nm, respectively. The diffraction grating of the LEOI-100 CCD spectrometer is set to the 600 L/mm. The resolution of the LEOI-100 CCD spectrometer is higher than the StellarNet's resolution, however, by using StellarNet we can examine spectral region with wavelength higher than 900 nm. These spectrometers are connected to a PC and emission spectrum is recorded with the software provided. The holder is positioned in front of the slit of the LEOI-100 spectrometer. By following the same steps applied in the Current-Voltage Characteristics part, dc plasma is generated.

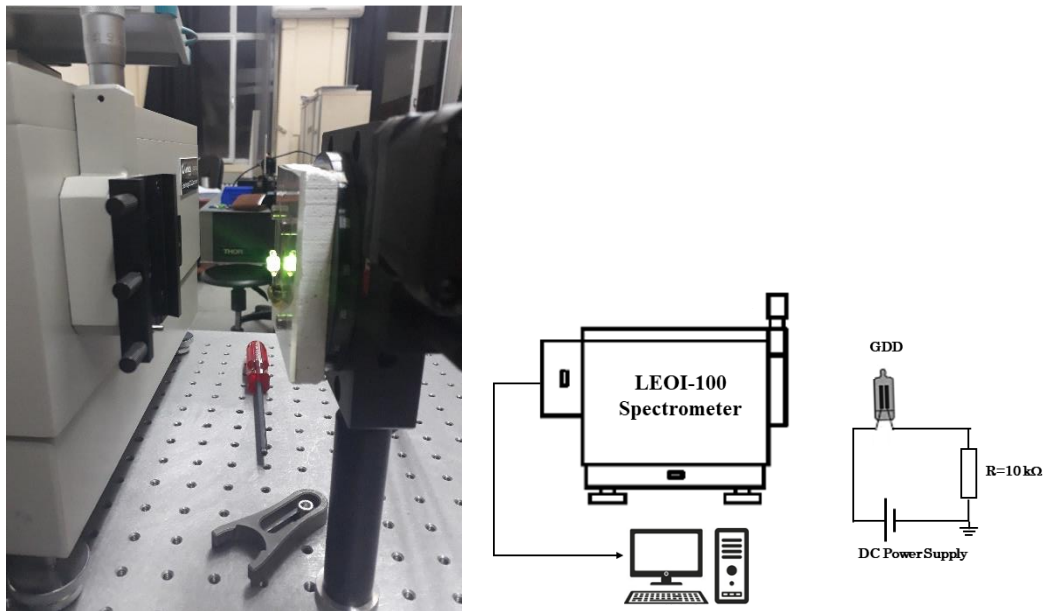


Figure 3.3: Photograph and schematic diagram of the experimental setup for examining the emission spectrum.

In this case, the ballast resistor of the circuit has a value of 10 k $\Omega$  and the current value is read from the dc power supply instantaneously. As a reference, the emission spectrum is recorded when the plasma is off. After the breakdown of plasma, the emission spectrum of the dc plasma at different current values are recorded. Then the reference data is subtracted from these measurements to obtain data that is purged from the side effects such as the background emission.

### 3.2. GDD-Millimeter wave detection

The detection performances of N523 and N520A are studied using a continuous mm-wave measurement system (Figure 3.4). The millimeter wave radiation is generated using a VDI frequency multiplier source (WR2.8AMC), driven by a frequency tunable Yttrium Iron Garnett (YIG) oscillator. The source was modulated electronically providing a frequency tunable output in the 82-125 GHz. The TTL output of the function generator which generates  $\pm 5$  V ac signal connected to the VDI multiplier source and used to modulate source in the required frequency. To control the output frequency of the mm-wave source, LabVIEW code is used. The output power of the source is in between 15-30 mW depending on the output frequency. The modulation frequency of source is chosen as 700 Hz. The TPX lens is used to collimate the incoming electromagnetic radiation and is placed 15 cm away from the mm-wave source. Teflon lens which has 10 cm focal length is used to focus the incoming radiation on the gap of electrodes. The spot size of the beam at focus depends on the frequency of the electromagnetic radiation. The spot size at the focus,

$$2w_0 \cong \frac{4\lambda f}{\pi D} \quad (3.2)$$

where  $\lambda$  is the wavelength of the beam,  $f$  is the focal length of lens and  $D$  is the diameter of the lens. We assume that beam fills the area of the lens. The theoretical value of the spot size changes from 6.1 mm to 9.3 mm according to the output frequency of the source.

The holder of GDD is rotatable. The polarization of the electromagnetic radiation is in y-direction. The influence of the polarization of the electromagnetic radiation on the detected signal is studied using the same experimental setup.

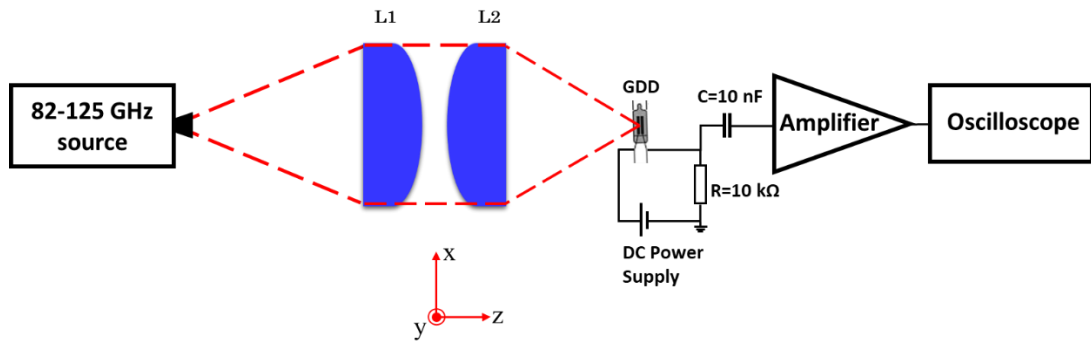


Figure 3.4: Schematics of the experimental setup for studying GDD detection dependence on the discharge current and the frequency of the incident radiation. L1 is the TPX lens (50 mm diameter, F#3) and L2 is the teflon lens (50 mm diameter, F#2).

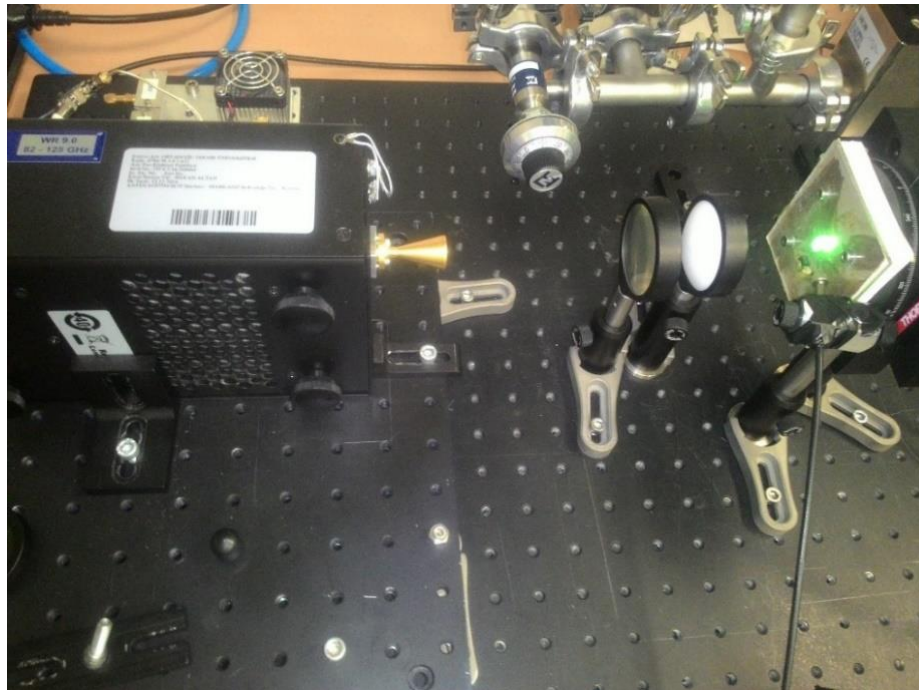


Figure 3.5: Photograph of the experimental setup demonstrated to study GDD-mm-wave interactions.

The change in the plasma current due to the incident electromagnetic radiation is measured by using ac-coupled non inverting amplifier circuit. The oscilloscope is used to monitor the detected signal. The schematics of the electric circuit used in the detection process is presented in Figure 3.6. The detection circuit is designed and simulated using NI Multisim software. As an operational amplifier, OPA 627 model is used which has lower noise, higher speed and lower offset voltage. The gain-bandwidth product of OPA627 is 16 MHz, which allows us to design amplifier circuit with high gain at low frequencies. Amplifier circuit with the gain of 83 is designed and well suited to our application.

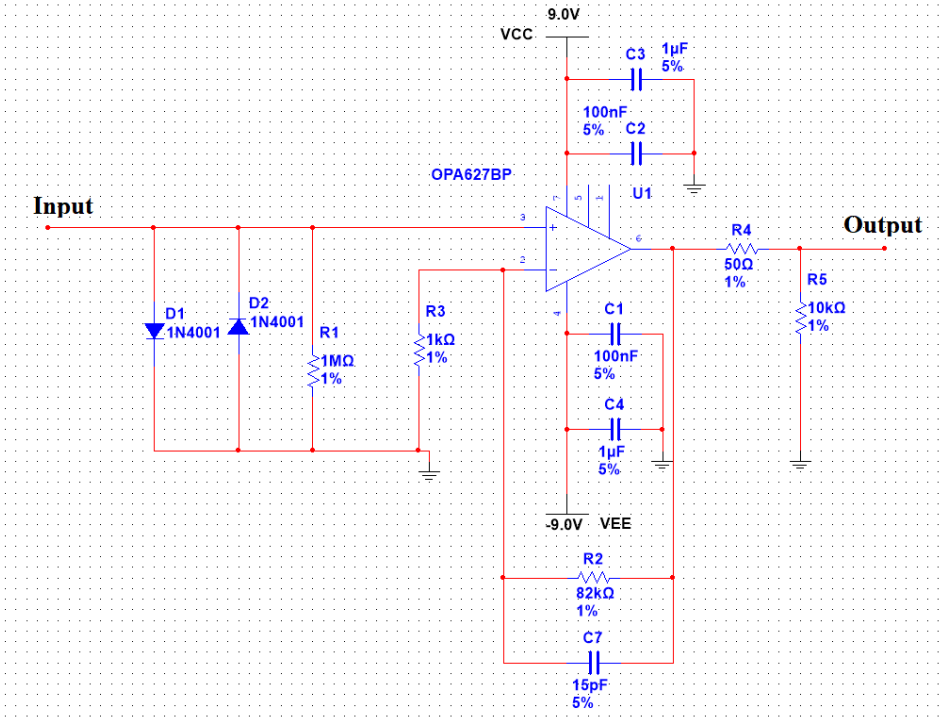


Figure 3.6: Schematics of the amplifier circuit for detection purposes.

The 10 nF capacitor is used to separate ac modulated signal which is obtained from the interaction of the plasma and the incoming electromagnetic radiation from the dc bias voltage. Two diodes are used to protect operational amplifier from sudden dc voltage fluctuations in plasma. The decoupling capacitors (C<sub>1</sub>, C<sub>2</sub>, C<sub>3</sub>, C<sub>4</sub>) are used to improve stability of operational amplifier. These capacitors should be placed as close as possible to the pins of the operational amplifier. The 15 pF capacitor is used to filter high frequencies that can affect the performance of operational amplifier. The

performance of the amplifier circuit is tested. The Multisim NI software provide the bode-plot of the designed amplifier circuit and presented in Figure 3.7. Furthermore, constructed circuit is tested by using a function generator and an oscilloscope. The response of the circuit is flat from 30 Hz to 7 kHz. The performance of the circuit is shown in Figure 3.8.

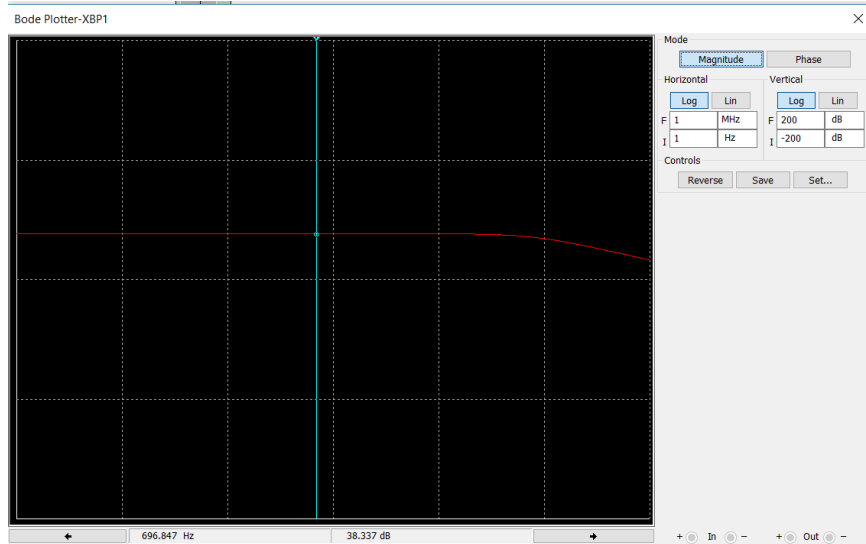


Figure 3.7: The response of the designed amplifier circuit as a function of frequency. The gain of the circuit is found as 38.2 dB at frequency about 700 Hz.

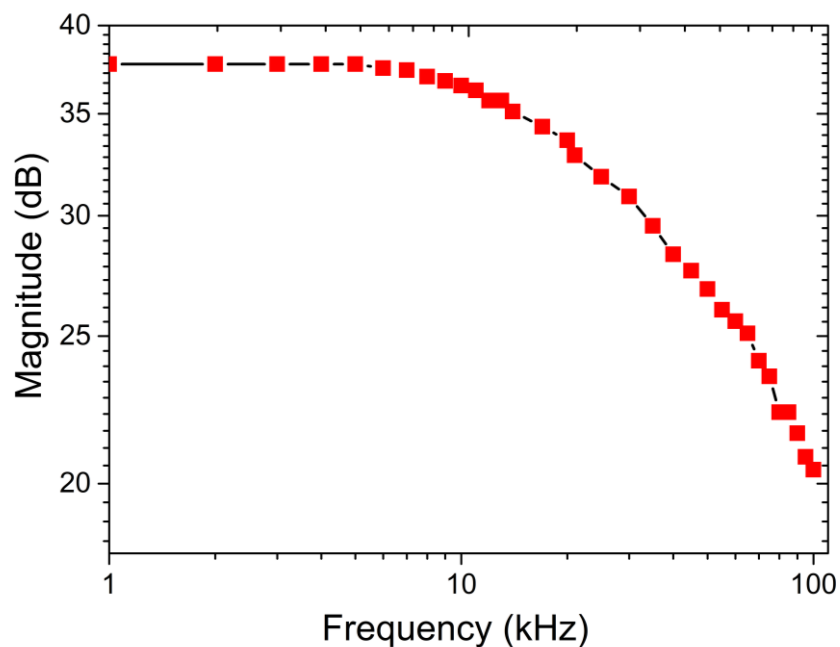


Figure 3.8: The response of the designed amplifier circuit as a function of frequency. The gain of the circuit is found as 37.7 dB at frequency about 700 Hz.

### 3.3. GDD as a single pixel detector

In the imaging experiment, the same mm-wave source is used. N 523 is used as a single pixel detector. GDD is placed at a position that the polarization of the incident radiation and the electric field in the GDD are parallel in order to get the maximum response. The image of “F” is obtained by the raster scan method using motorized xy-scanning stage. The “F” shaped object is placed on the motorized stage. LabVIEW code is used to control motorized stage and to obtain image as shown in Figure 3.9.

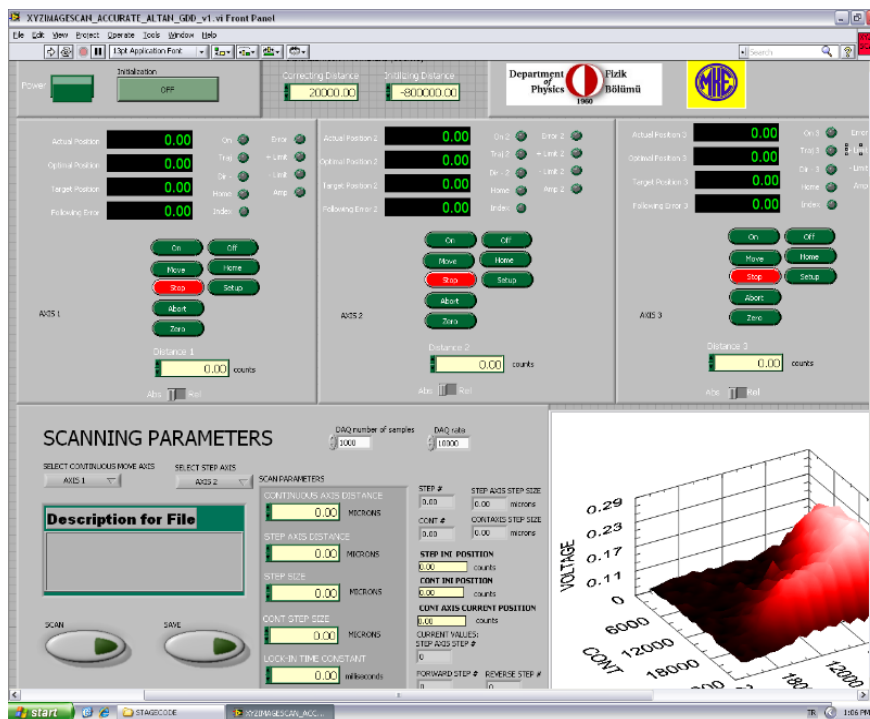


Figure 3.9: Front panel of the LabVIEW code used to control motorized stage and collect data.

The two dimensional area of the sample is divided into pixels as shown in Figure 3.10. The step size of the motorized scanning stage is set as 1 mm in both x and y directions. Both the length and width of the scanned area is 24 mm. The point where the scanning process began is specified as the origin of the xy-graph presented in Figure 3.10. At the beginning, the origin of the xy-graph is placed at the focus of the L2 lens. First, the stage moves along the x-direction. The stage stops when it reaches to the top point (1 mm, 24 mm) in the x direction and then moves to the next row. And it starts to scan in downward direction with the 1 mm step size. The scanning procedure continues in

this way until the scan of the whole area is completed. The total number of pixel scanned is 576. The distance between motorized stage and L2 lens is 10 cm. The middle of the “F” shape is empty and rest of sample covered with aluminum foil. The focused electromagnetic radiation transmits through the empty portion of the sample. The electromagnetic radiation reflects when it faces with the aluminum portion of the sample. Then by using a set of Teflon lenses shown in Figure 3.11, transmitted radiation is focused on the electrode gap of the GDD. The detected signal is amplified using the circuit and the output of the amplifier circuit is connected to the DAQ to transmit data to the PC. DAQ rate of samples is set as 10000, since the modulation frequency is 700 Hz. By using LabVIEW, detected signal at each step is recorded and an image of the object is obtained. The 24X24 mm area is scanned to obtain an image and it takes about 40 minutes.

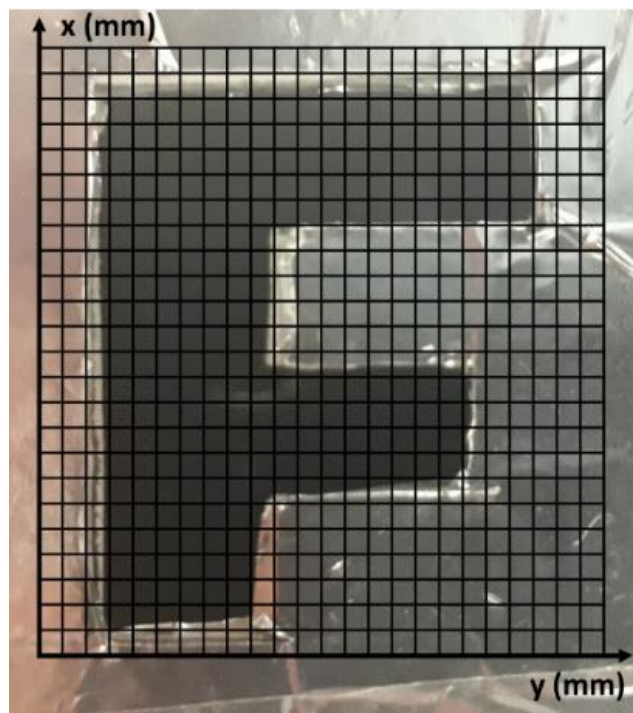


Figure 3.10: Photograph of the 24X24 pixel “F” shaped object.

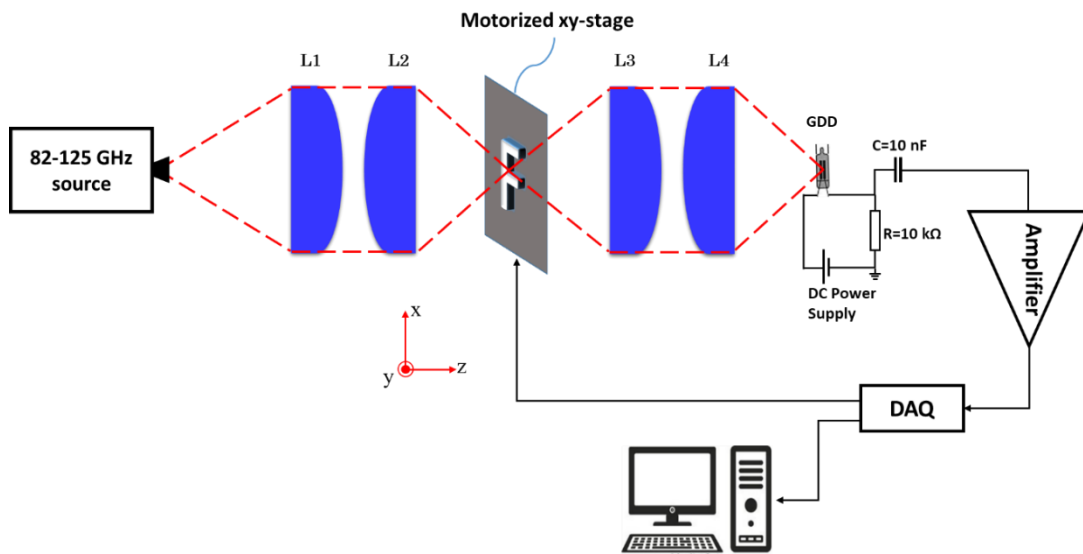


Figure 3.11: Schematics of the raster scan mm-wave imaging system. L1 is the TPX lens (50 mm diameter, F#3). L2, L3 and L4 are teflon lens (50 mm diameter, F#2).



Figure 3.12: Photograph of the experimental setup for imaging applications.

## CHAPTER 4

### EXPERIMENTAL RESULTS AND DISCUSSION

#### 4.1. Plasma Characterization

##### 4.1.1. Current-Voltage (I-V) Characteristics measurements

The voltage current characteristics of the dc discharge obtained in N523 and N520A is presented in Figure 4.1 and Figure 4.2. The voltage drop on the plasma is calculated using equation the 3.1 written in measurement part. The current through the dc discharge is controlled by the voltage adjustable power supply. Breakdown of the plasma depends on the distance between electrodes, electrode geometry and gas pressure. The breakdown voltages of these lamps are nearly the same, around 61 V. The current through the circuit is varied by changing the voltage of the dc power supply. When the breakdown occurs, the current through the plasma is measured as 2.4 mA. The I-V characteristics of two lamps are examined for the current in the range of 2.4-20 mA and the dc voltage observed in 61-70 V range. The generated plasmas are stable in those range. The dc voltage on the plasma increases with the increasing applied current which means the examined plasma is in the abnormal mode. In case of the abnormal mode, the slope of the I-V characteristics graph is positive ( $\Delta V/\Delta I > 0$ ). Townsend, subnormal and normal modes are not observed in this current range. The mode of the glow discharge can be controlled using a ballast resistor. To study modes before the abnormal mode, the higher resistor should be used. For higher current values, the arc mode can be observed. The highly luminous layer is called the negative glow region observed near the cathode. The negative glow covers the entire cathode.

The negative glow region is followed by the non-luminous region called the Faraday dark space. Since the anode and cathode are close to each other, positive column region cannot be observed at low pressure discharge.

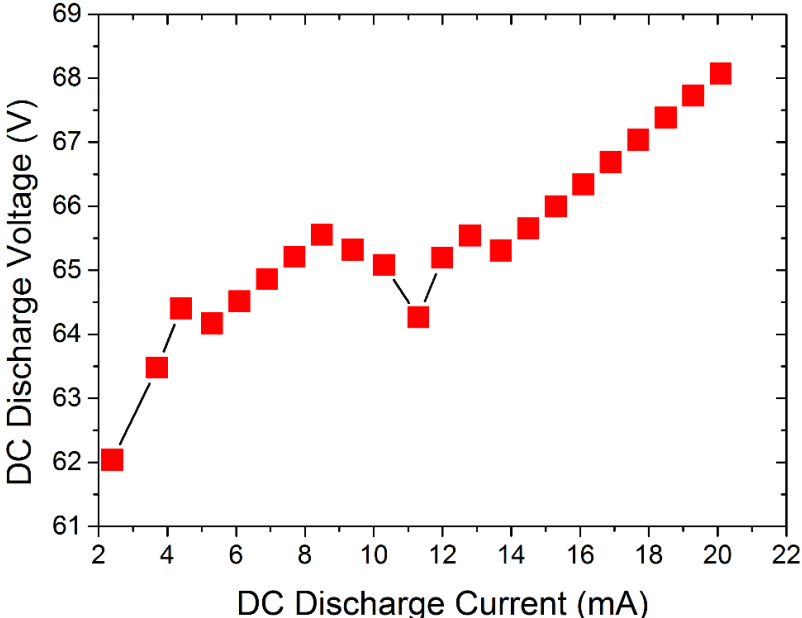


Figure 4.1: Measured DC voltage between the electrodes of N520 A as a function of the discharge current.

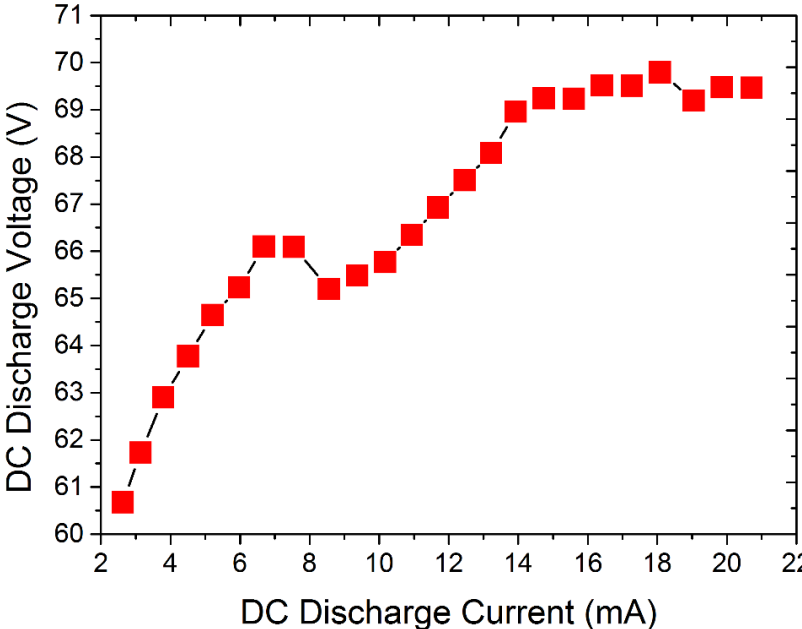


Figure 4.2: Measured DC voltage between the electrodes of N523 as a function of the discharge current.

Since the voltage drop on the plasma and the current through plasma are known, the resistance of the plasma is measured and presented in Figure 4.3 as a function of the current. It is clear that plasma becomes more conductive at high current values. Increase in the current leads to generation new free electrons which plays an important role in increasing conductivity of plasma. Just after breakdown, the plasma resistance is about 26 k $\Omega$  and it decreases to 4 k $\Omega$  at 20 mA.

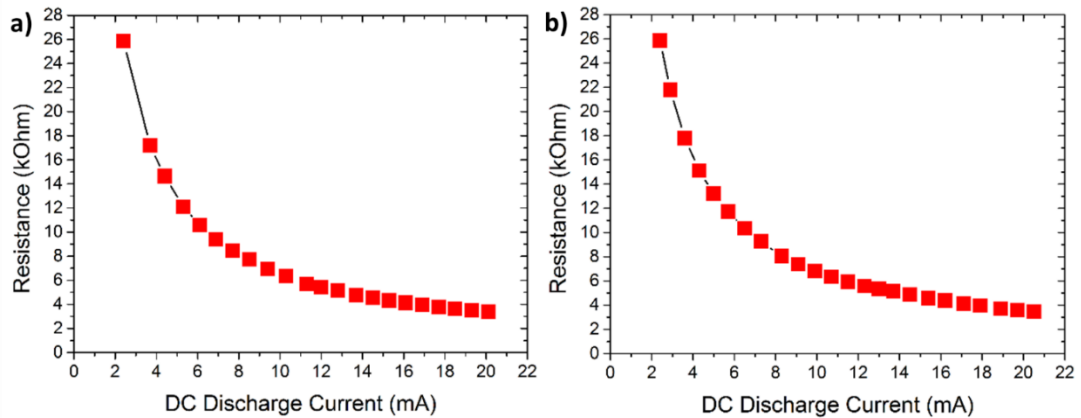
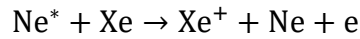


Figure 4.3: The resistance of the generated dc glow discharge inside a) N523 and b) N520A as a function of the discharge current.

#### 4.1.2. Optical Emission Spectroscopy measurements

Optical Emission Spectroscopy is used to determine the plasma parameters of these commercial glow discharge lamps. The emission spectrum of the glow discharge lamps is obtained for different current values by using the experimental setup presented in Figure 3.3. Emission spectrum of the N520 at 9 mA discharge current is recorded in the spectral region from 580 nm to 730 nm as shown in Figure 4.4. Twenty five well resolved Ne I emission lines are observed in the emission spectrum and means N520A contains only neon species. In order to test the emission spectrum of the N523 two spectrometers are used. The StellarNet spectrometer is used since it can scan wavelengths regions higher than 730 nm. It is found that the N523 contains penning mixture of neon and xenon. In Figure 4.6, we observe seven xenon lines in the spectrum between 800 nm and 1000 nm. Green phosphor emission curve is also observed between 500 nm and 575 nm of the region of the spectrum due to phosphor

coating inside N523 discharge lamp. The N523 discharge lamp is studied using LEOI-100 spectrometer to achieve higher resolution in the region from 580 nm to 730 nm. In Figure 4.5, the emission spectrum of the N523 is presented at 9 mA discharge current. Beside the emission lines of the neon species, three xenon lines are recorded. The main inert gas used in discharge lamp is neon. Xenon gas is employed to enhance discharge inside lamp. The metastable energy of the neon is 16.6 eV and higher than the first ionization energy of the xenon which equals to 12.1 eV. The penning ionization reaction of Ne-Xe mixture can be written as,



According to the patent about the glow lamps [38], neon.-xenon penning mixture lamps contains 0.001-1 percent of xenon and rest is neon. The need of obtaining penning mixture is often to lower the breakdown voltage of the plasma discharge. However, in this case we find the breakdown voltage of both lamps are near 61 V. It can be concluded that xenon has not changed the breakdown voltage of the penning mixture which is consistent with information given in the patent [38]. On the other hand, the use of the xenon in such application is necessary to increase the expected life time of the lamp. All neon emission lines observed in this spectral regions are due to the transitions from  $2p^53p$  configuration to the  $2p^53s$  configuration level. Spectroscopic details of the recorded neon and xenon lines such as wavelengths, statistical weights, excitation energies and transition probabilities are listed in Table 4.1.

Table 4.1: Spectroscopic details of observed xenon and neon lines. The data is taken from the NIST database.

Species	$\lambda$ NIST (nm)	$E_i$ (eV)	$E_k$ (eV)	$g_i$	$g_k$	$A_{ki}$ ( $10^8 \text{ s}^{-1}$ )
Ne I	585.25	16.85	18.97	3	1	0.682
Ne I	588.19	16.62	18.73	5	3	0.115
Ne I	594.48	16.62	18.7	5	5	0.113
Ne I	597.55	16.62	18.69	5	3	0.0351
Ne I	602.99	16.67	18.73	3	3	0.0561
Ne I	607.43	16.67	18.71	3	1	0.603
Ne I	609.61	16.67	18.7	3	5	0.181
Ne I	614.3	16.62	18.64	5	5	0.282
Ne I	616.35	16.72	18.73	1	3	0.146

Ne I	621.73	16.62	18.61	5	3	0.0637
Ne I	626.64	16.72	18.69	1	3	0.249
Ne I	630.47	16.67	18.64	3	5	0.0416
Ne I	633.44	16.62	18.58	5	5	0.161
Ne I	638.47	16.67	18.61	3	3	0.321
Ne I	640.22	16.62	18.56	5	7	0.514
Ne I	650.65	16.67	18.58	3	5	0.3
Ne I	653.28	16.72	18.61	1	3	0.108
Ne I	659.89	16.85	18.73	3	3	0.232
Ne I	667.83	16.85	18.7	3	5	0.233
Ne I	671.7	16.85	18.69	3	3	0.217
Ne I	692.94	16.85	18.64	3	5	0.174
Ne I	703.24	16.62	18.38	5	3	0.253
Ne I	717.39	16.85	18.58	3	5	0.0287
Ne I	724.71	16.67	18.38	3	3	0.0935
Xe I	682.73	9.45	11.26	1	3	
Xe I	688.24	9.686	11.49	5	7	
Xe I	711.9	9.721	11.46	7	9	
Xe I	823.38	8.315	9.821	5	5	
Xe I	882.18	8.315	9.721	5	7	
Xe I	895.47	8.437	9.821	3	5	
Xe I	904.79	8.315	9.686	5	5	
Xe I	916.51	8.437	9.789	3	3	
Xe I	980.23	8.315	9.58	5	3	
Xe I	992.59	8.437	9.686	3	5	

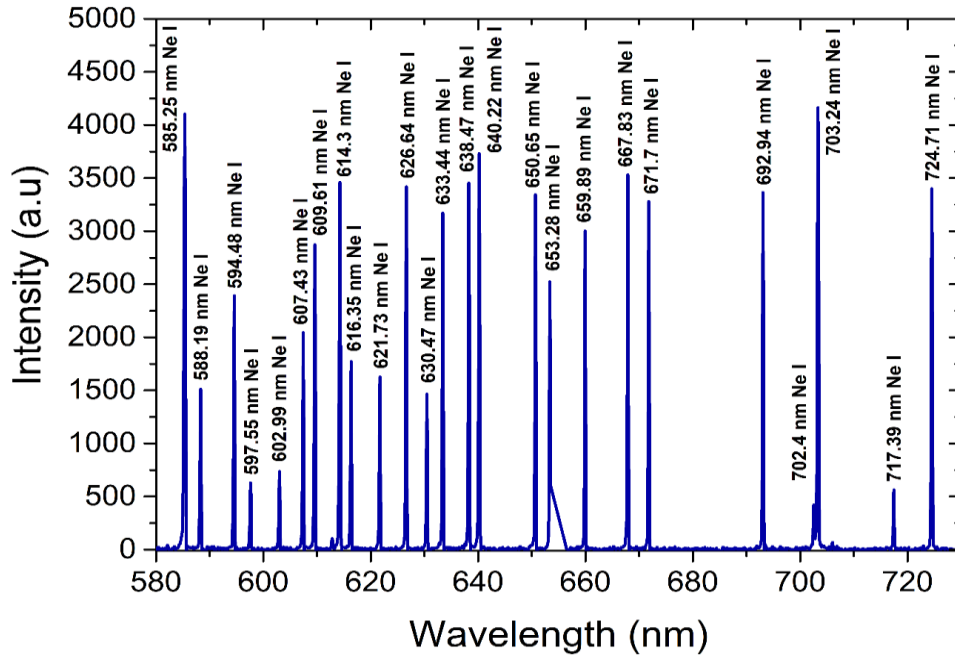


Figure 4.4: Experimental emission spectrum of N520A recorded in the spectral region from 580 nm to 730 nm at 9 mA. The line intensity profile is obtained by using LEOI-100 CCD spectrometer.

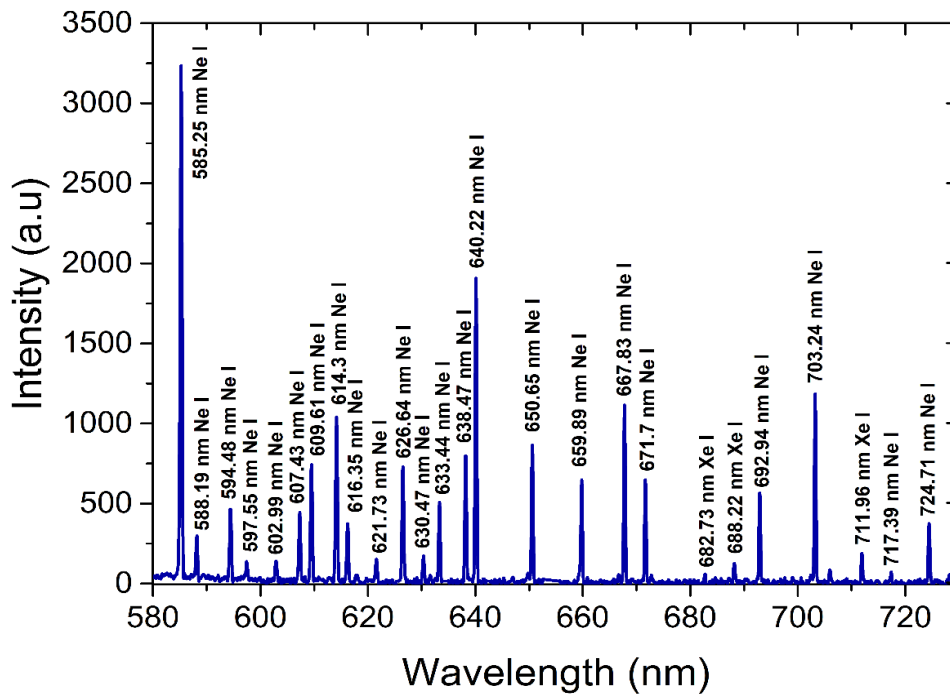


Figure 4.5: Experimental emission spectrum of N523 recorded in the spectral region from 580 nm to 730 nm at 9 mA. The line intensity profile is obtained by using LEOI-100 CCD spectrometer.

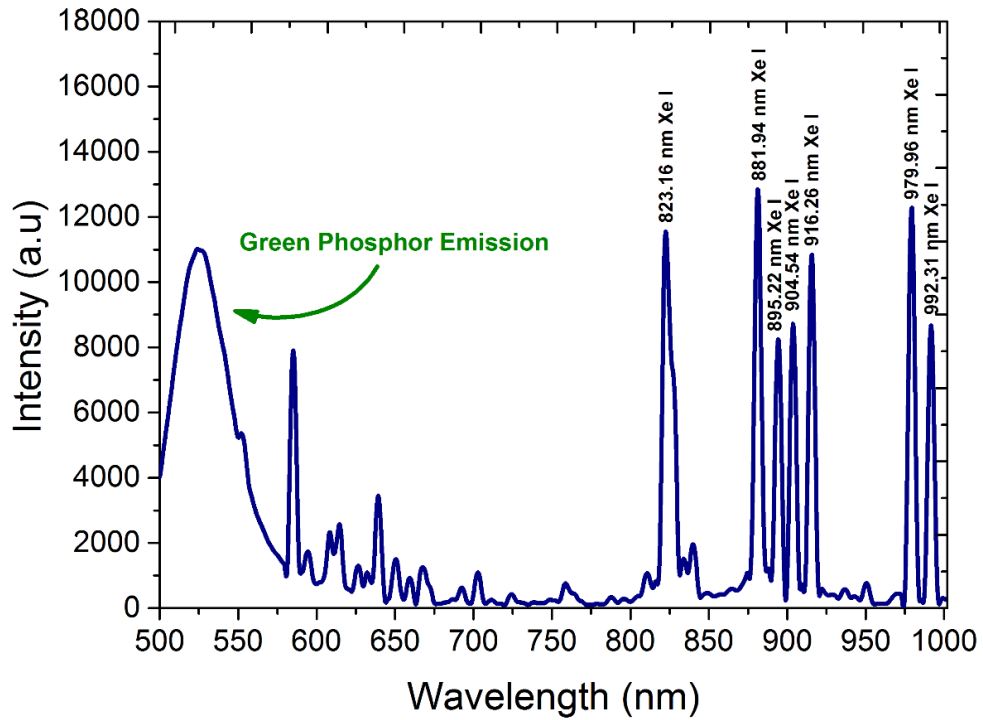


Figure 4.6: Experimental emission spectrum of N523 recorded in the spectral region from 500 nm to 1000 nm at 9 mA. The line intensity profile is obtained by using StellarNet spectrometer.

Figure 4.7 presents the behavior of the emission line intensities of selected three neon species (626.64 nm, 640.21 nm and 703.29 nm) as a function of the discharge current for N520A and N 523, respectively. The discharge current tuned within 1 mA steps by varying the voltage of the dc power supply. The intensities of the selected lines are recorded for the discharge current from 1.5 mA to 9 mA. It can be clearly seen that, the intensity of the selected emission lines increase with increasing discharge current. The relation between intensity and discharge current is found as linear for these wavelengths. The electrons gain enough energy from the field which increases with the increase of the applied voltage. These electrons participate in the excitation and the ionization processes which lead to increase in the electron density. Discharge current increases because of newly generated electrons and it leads to increase in the intensity of the line [39-40].

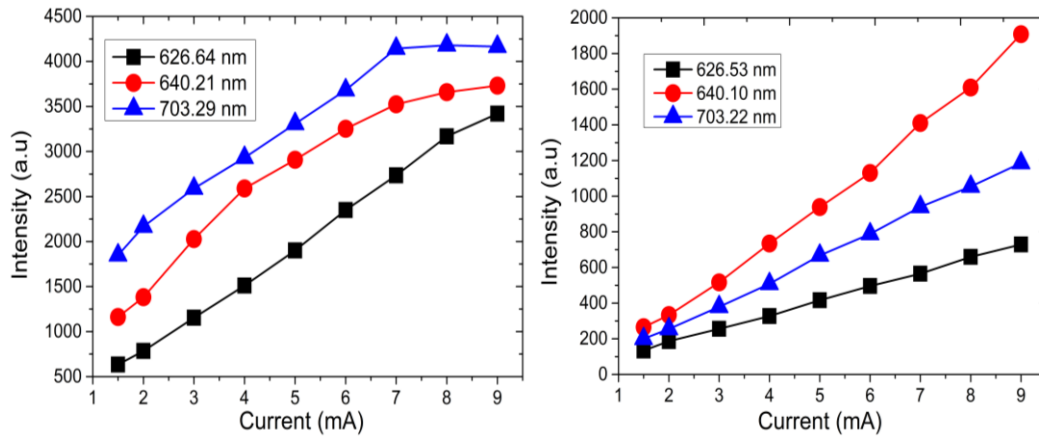


Figure 4.7: Intensity of three neon lines as a function of discharge current for a) N520A and b) N 523.

#### 4.1.2.1. Measurements of electron temperature and electron density

The Boltzmann plot method is the one of the practical ways to calculate the electron temperature. The spectral lines which have a larger difference in their upper energy level should be chosen to improve the accuracy of this method. Intensity and spectroscopic data of the spectral lines listed in Table 4.1 are used to construct the Boltzmann plot. The eight Ne I lines are used to calculate the electron temperature of the discharge: 588.19 nm, 597.55 nm, 602.99 nm, 626.64 nm, 630.47 nm, 653.28 nm, 659.89 nm, 671.7 nm and 724.71 nm. Figure 4.8 shows the Boltzmann plot of the N520A discharge lamp operating at 9 mA discharge current. The electron temperature is deduced from the slope of the Boltzmann plot as 0.28 eV. The electron temperature of the N523 discharge lamp at 9 mA is determined as 0.42 eV. In this case, six Ne I lines (594.48 nm, 607.43 nm, 609.61 nm, 638.47 nm, 703.24 nm and 724.71 nm) are used to construct Boltzmann plot is shown in Figure 4.9. The electron temperature of the N 523 is higher than N 520A's at 9 mA discharge current. The calculated electron temperature values are in the range of electron temperature for low pressure glow discharge. The largest difference between the upper energy levels of the selected lines is 0.34 eV for both N 520A and N 523. The error in the electron temperature is mainly because of errors in transition probabilities and measured signal intensity.

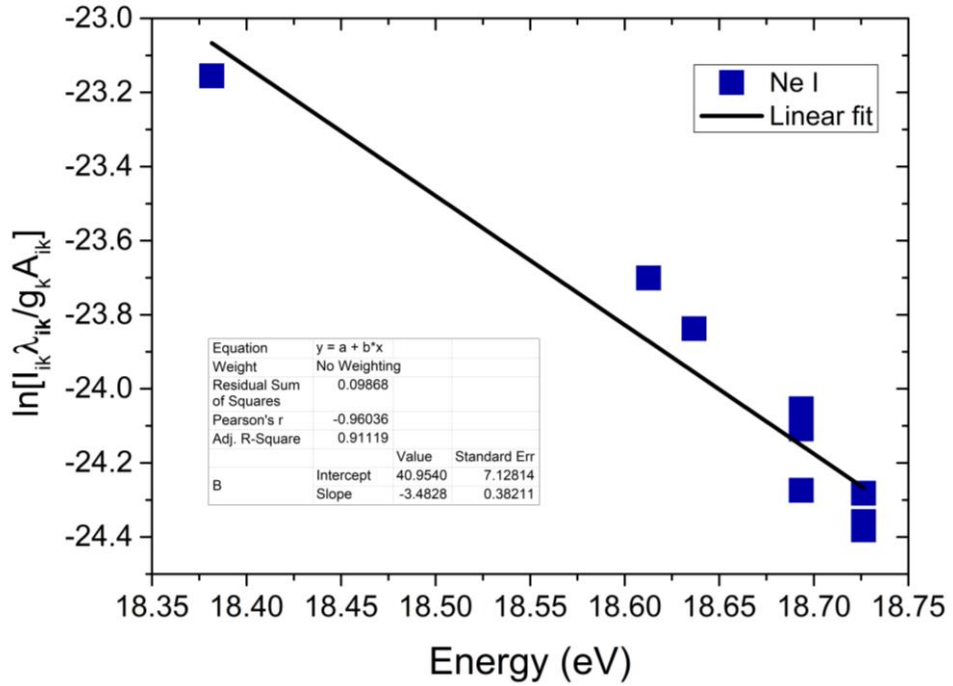


Figure 4.8: Boltzmann plot to calculate the electron temperature of the dc glow discharge plasma inside N 520A at 9 mA.

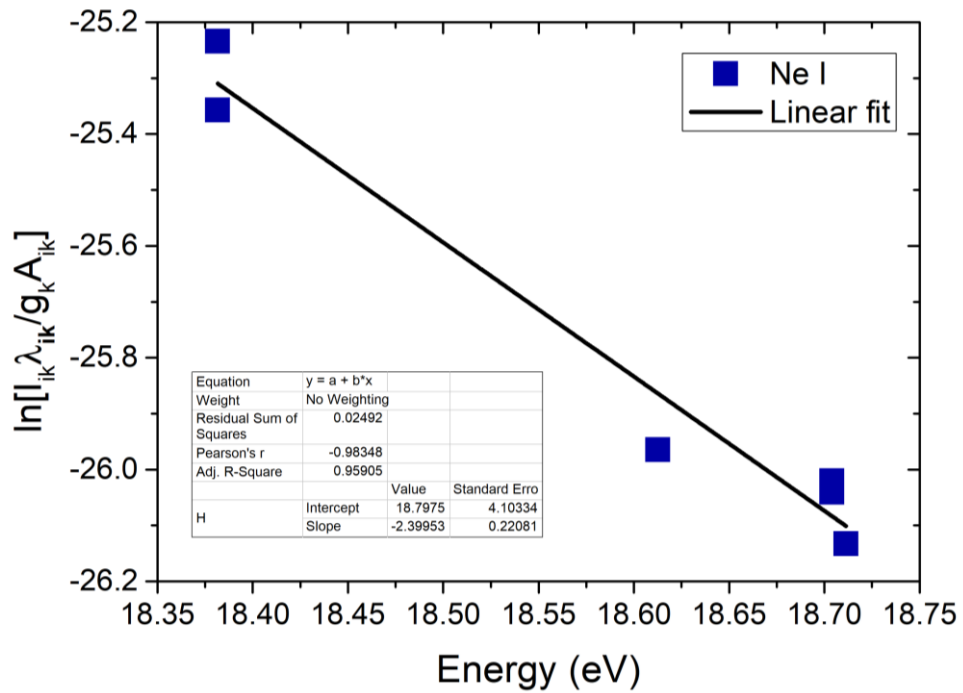


Figure 4.9: Boltzmann plot to calculate the electron temperature of the dc glow discharge plasma inside N 523 at 9 mA.

The electron density of the generated dc discharge can be measured by using Stark broadening method. The full width at half maximum (FWHM) of the selected broadened line for both discharge lamp are determined. The electron density is calculated by using equation 2.13.

$$n_e = \frac{\Delta\lambda_{1/2}}{2w} \times 10^{16}$$

The value of the electron impact factor for different wavelengths are listed in Grimm's book and depend on the electron temperature of discharge. It can be clearly seen that the electron density is proportional with the FWHM of selected line. The resolution of the used spectrometers is not sufficient to measure real FWHM of the line because of the effect of the instrumental broadening. However, we can compare the electron densities of the two discharge lamps at required discharge current. In order to investigate the difference between electron densities of the two discharge lamps, we choose the neon line 585.25 nm to obtain FWHM. The FWHMs for two discharge lamps are deduced by fitting the line profile with Voigt function, since the best fit obtained by Voigt curve rather than Lorentz curve. The typical Voigt fitting profile of Ne I at 9 mA discharge current is shown in Figure 4.10 and Figure 4.11 for N520A and N523, respectively. The FWHM of the line is measured as 0.33 nm for N520A discharge lamp and 0.39 nm for the N523 discharge lamp. Since the FWHM of the N523 is higher than the N520A's, it can be concluded that the electron density of the N523 is higher as expected.

The exact value of the electron density of the discharge lamps cannot be obtained, since the instrumental FWHM cannot be measured. It can be done by measuring FWHM of laser source which has peak wavelength close to interested wavelength region. In our case, He-Ne laser can be used since its peak wavelength is about 632 nm. The real FWHM can be deduced from the subtraction of FWHM's of discharge and He-Ne laser.

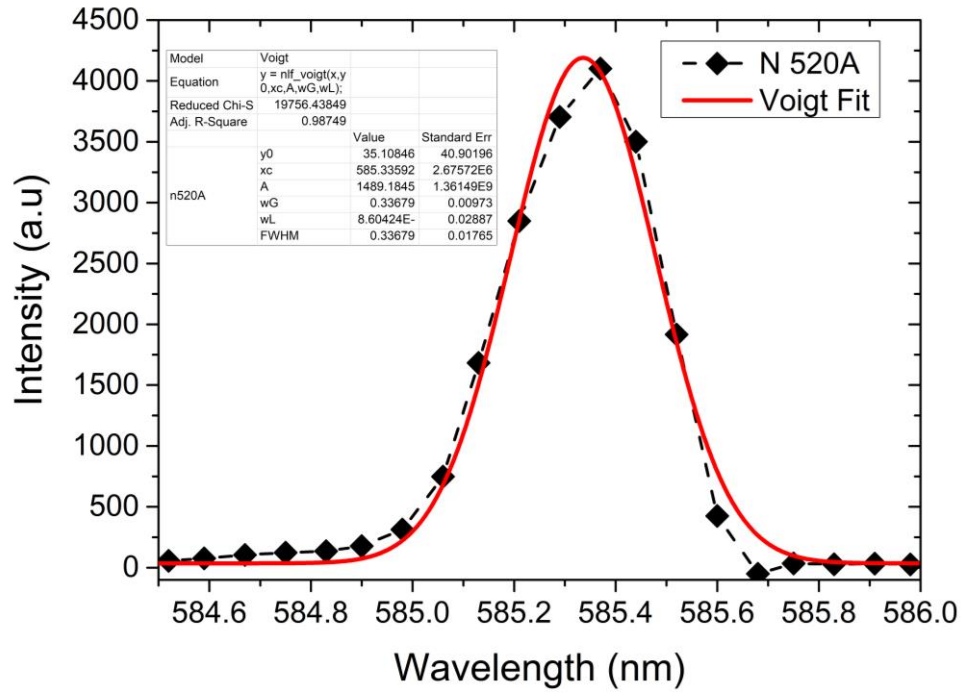


Figure 4.10: The stark broadened profile of the Ne I line at 585.25 nm for N520A discharge lamp. The red line is the Voigt fit of the experimentally observed profile.

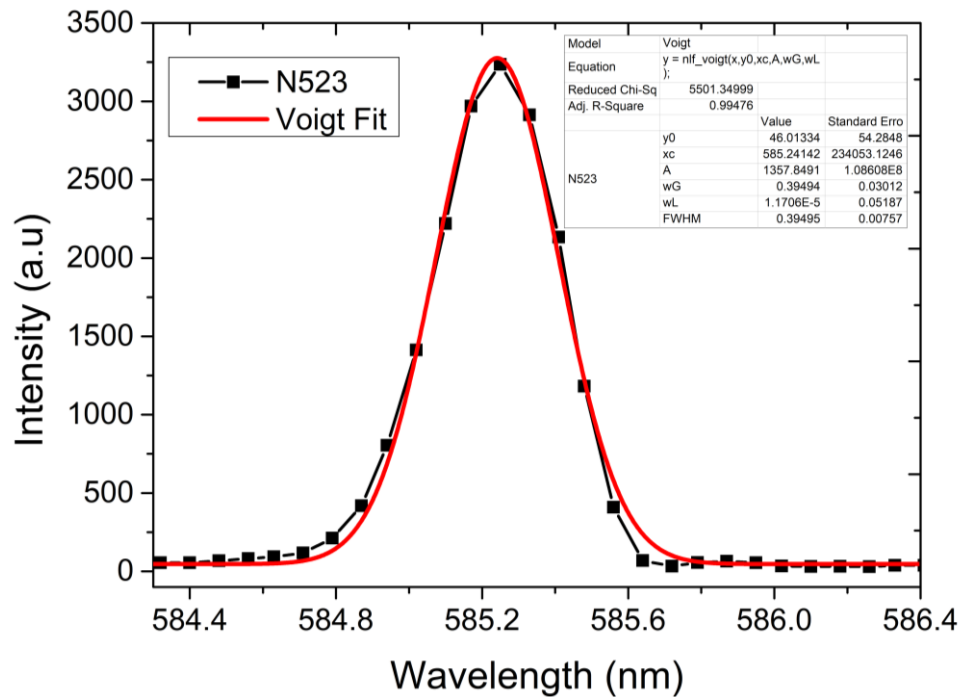


Figure 4.11: The stark broadened profile of the Ne I line at 585.25 nm for N523 discharge lamp. The red line is the Voigt fit of the experimentally observed profile.

## 4.2. Responsivity of the GDD

The experimental setup presented in Figure 3.5 is designed to study interactions between mm-wave radiation and a GDD. First, the effect of the discharge current on the response of the GDD is investigated at different radiation frequencies such as 87 GHz and 100 GHz. The output power of VDI multiplier source (WR2.8AMC) at 87 GHz and 100 GHz radiation is measured using a Golyay Cell and found as 23.5 mW and 25 mW, respectively.

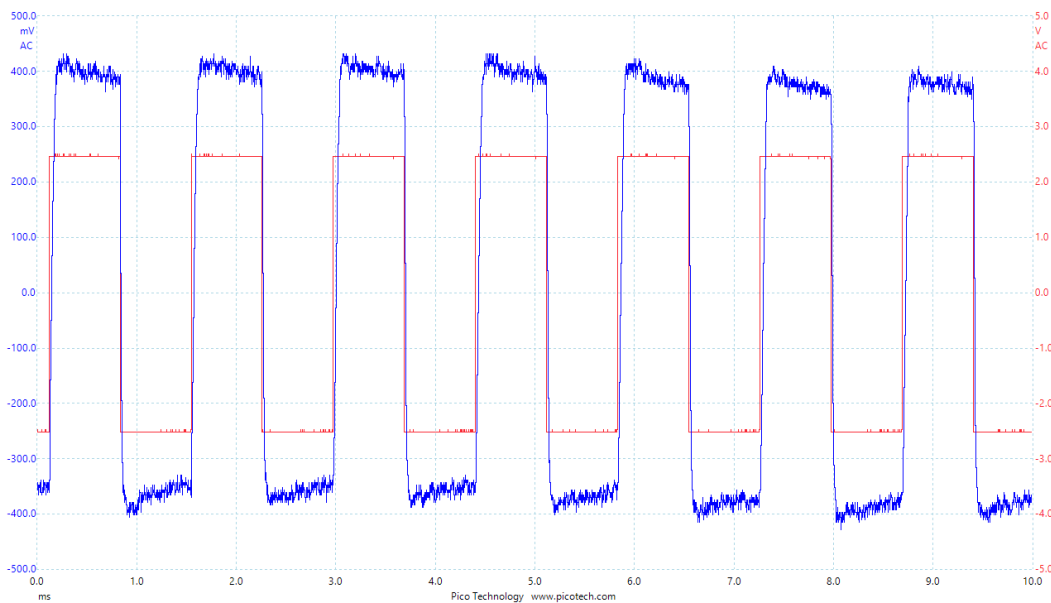


Figure 4.12: Blue line is the detected signal by GDD and red line is the TTL modulation signal given by function generator to modulate mm-wave source. Modulation frequency is 700 Hz.

Glow discharge process begins with applying sufficient dc voltage between the electrodes of the discharge lamps. Then the discharge current is tuned with 1 mA steps by using voltage regulated DC power supply. The modulation frequency of the mm-wave source is set to 700 Hz. The detected signal (blue line) at 87 GHz and TTL modulation signal (red line) are shown in Figure 4.12. Two signals are in phase.

The responsivity as a function of the discharge current for both N523 and N520A discharge lamps are given in Figure 4.13 and Figure 4.14. The discharge

current is chosen in the range from 2 mA to 9 mA and the discharge lamps operate in the abnormal glow mode. The detected signal increases with the increase in the discharge current at all radiation frequencies for both discharge lamps and has sharp increase for the discharge current values higher than 6 mA. Since these discharge lamps operate at the abnormal glow mode, most atoms are in the excited state. Most of the ionization of atoms processes are observed at the cathode dark space where the total electron energy is at maximum. Most electrons are generated at the end of the cathode layer where the electric field begins to decay. At the cathode dark space region, the incident mm-wave radiation is absorbed by weakly bounded and free electrons. The absorption process leads to generate new free electrons and causes slight increase in the discharge current. The increase in the discharge current is proportional to the term [41],

$$\frac{nv}{(v^2 + w^2)}$$

where  $n$  is the electron density,  $w$  is the frequency of the incident radiation and  $v$  is the electron-neutral collision frequency. The optimum response occurs when the electron neutral collision frequency is equal to the frequency of the incident radiation. The electron-neutral collision frequency is directly proportional to the electron density. In previous section, we found that the electron density increases with the increasing discharge current. As a result, increase in the discharge current leads to the higher ionization inside the discharge. More electrons will have chance to interact with the incident mm-wave radiation. Generation of new electrons by absorption of mm-wave radiation is now easy in such environment. Thus the detected signal increases with the increase of the discharge current. So the detection mechanism of the mm-wave using a dc discharge is the enhanced cascade ionization which mostly take place at the cathode dark space region. The detection performance of the N523 discharge lamp is better than the N520A's performance. Gas components and coating inside lamps' glass are the main difference between N523 and N520A. The mixture of neon and xenon inert gases is used in the N 523 discharge lamp. However, the N520A discharge lamp contains only pure neon gas. It can be concluded that the use of the penning mixture

improves the detection performance of the GDD, since the penning mixture increases the electron density in the discharge lamp [42].

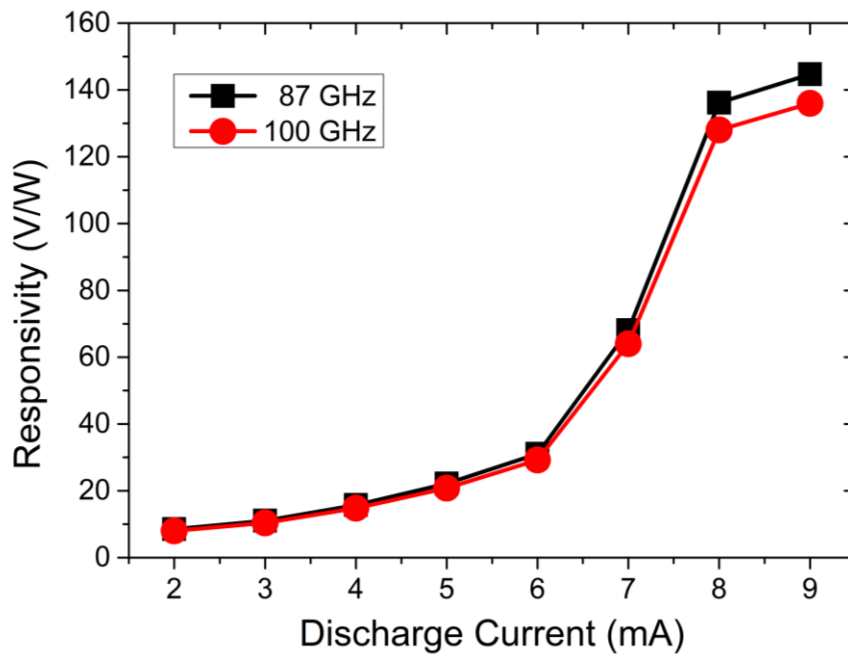


Figure 4.13: Responsivity of N523 as a function of the current at two different radiation frequencies.

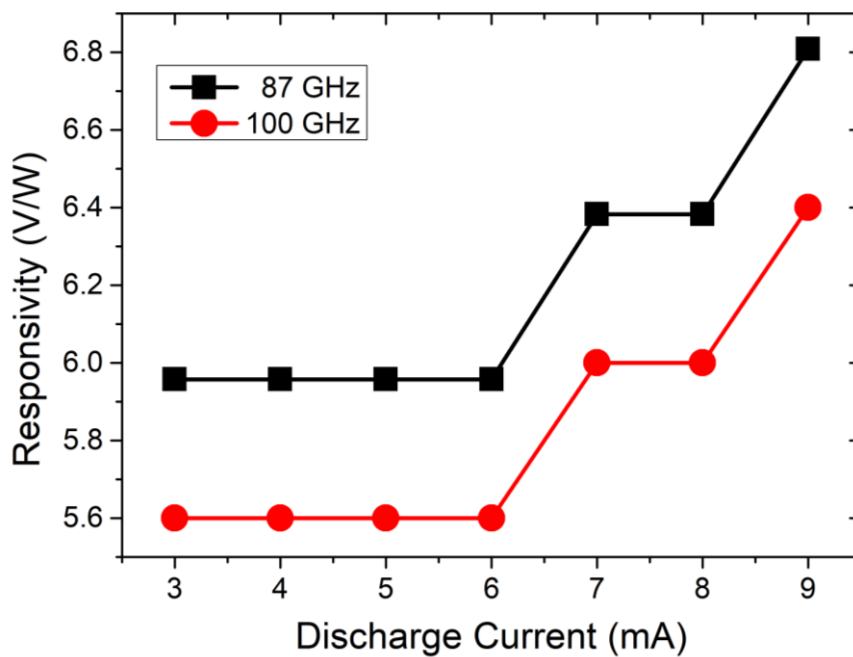


Figure 4.14: Responsivity of N520A as a function of current at two different radiation frequencies.

The phosphor coating has also positive contribution to the detection process. Electrons in the Faraday space and in the negative glow regions are diffused out toward the walls of the lamp, and they interact with the phosphor coating. Additional free electrons can be generated by the photoexcitation and the photoionization processes because of the phosphor coating. As a result, the N523 can be used as a single pixel detector in the mm-wave and THz region.

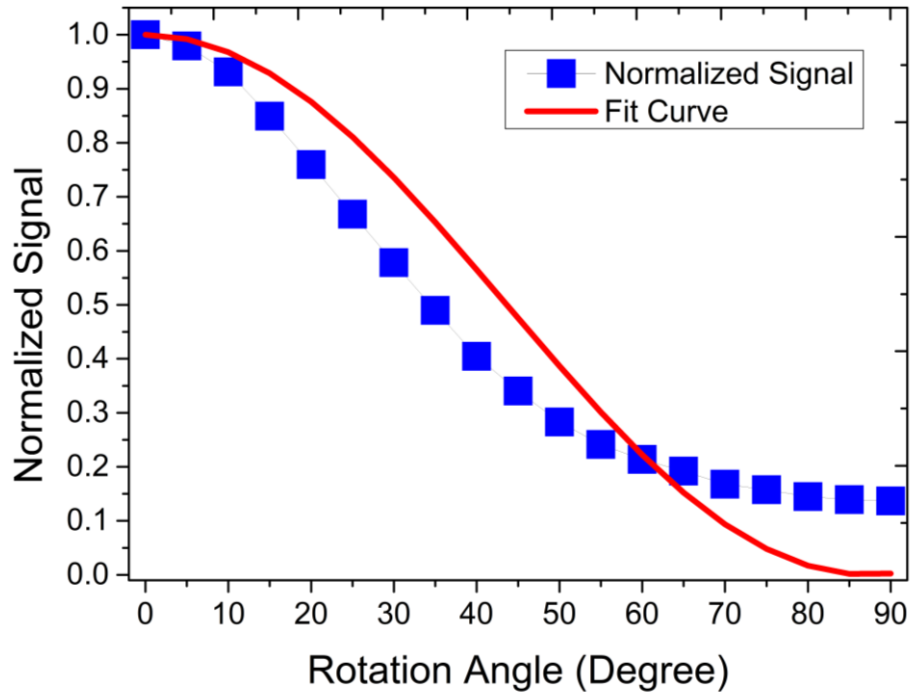


Figure 4.15: Normalized signal for a N523 discharge lamp with varying rotation angle. The red line shows the behavior as expected using Malus's law.

The N523 is used to investigate the dependence of the detected voltage signal on the polarization of the incident radiation. The holder is rotated within 5 degree steps and detected signal is recorded. Experiment is carried out when the frequency of the incident radiation is 87 GHz and the discharge current is 9 mA. Modulation frequency is 700 Hz. Figure 4.15 shows that maximum detected signal is obtained when the polarization of the electric field of the incident radiation is parallel to the polarization of the DC electric field inside the GDD. When the polarization of both electric fields are perpendicular, then the detected signal is minimum. Recorded data is normalized and fitted with respect to Malus' Law. Mismatch in the directions of both electric fields

effects the responsivity of the GDD. The electrons diffuse toward walls of the lamp when the electric fields are orthogonal which it leads to a decrease in the detected signal. However, if the electric field of the incident radiation oscillates in the polarization direction of the DC electric field, it increases the velocity of the electrons drifting towards the anode [43].

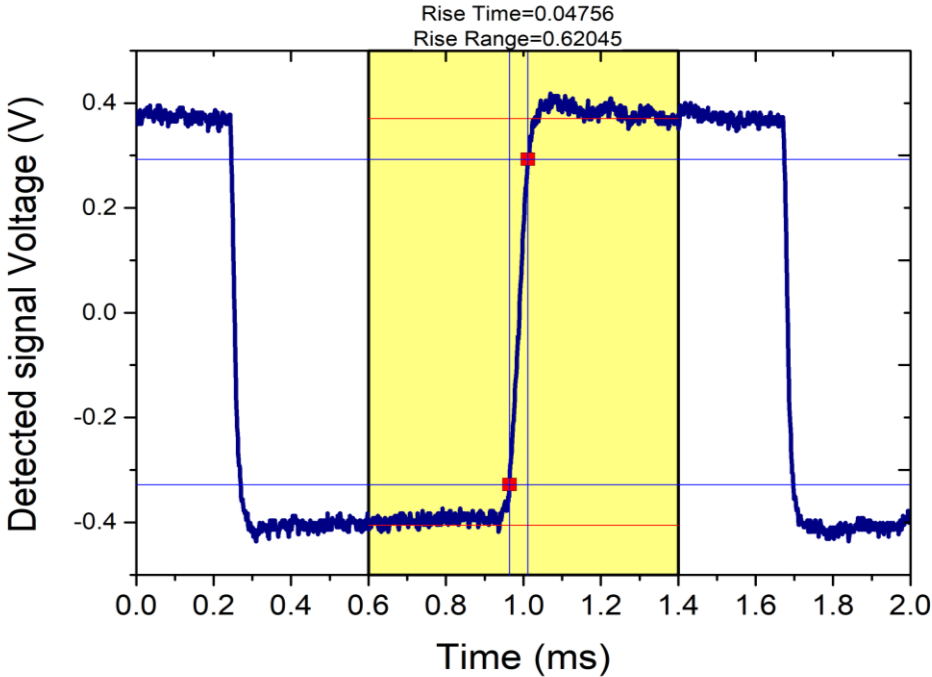


Figure 4.16: The waveform of the detected signal at 87 GHz and GDD operates at 6 mA discharge current.

The time required for the output signal to increase from the 10% point to the 90% point of the peak amplitude of the output signal is known as the rise time. The speed of response of the detectors are determined by measuring the rise time. To investigate the rise time of the GDD, the radiation of the frequency is set to the 87 GHz and discharge current is 6 mA. The waveform of the detected signal shown in Figure 4.16. The data is processed by using the Origin software. The rise time of the GDD with its readout circuit is found as roughly around 48 microsecond.

### 4.3 MM-wave imaging using GDD as a single pixel detector

The experimental setup used in the imaging is shown in Figure 3.12. Imaging is performed at three different radiation frequencies such as 87 GHz, 100 GHz and 119 GHz. The N523 discharge lamp is used as a single pixel detector due to its better performance than the N520A discharge lamp. Modulation frequency of incident radiation is 700 Hz. The discharge current of the GDD is chosen as 6 mA, since at higher currents the responsivity of the GDD decreases with time. The GDD is placed in such a position that the electric fields of the dc discharge and the incident radiation are in parallel. The theoretical spot size is calculated as 8.7 mm, 7.6 mm and 6.4 mm for the radiation frequencies 87 GHz, 100 GHz and 119 GHz, respectively. The obtained data is proceeded using an Origin software. The normalized mm-wave images are presented at the different radiation frequencies in Figure 4.17, Figure 4.18 and Figure 4.19. The aluminum foil reflects the mm-wave radiation and blue color part of images represents the reflected radiation. Since the resolution of the image depends on the radiation frequency, the best resolved image is obtained at 119 GHz.

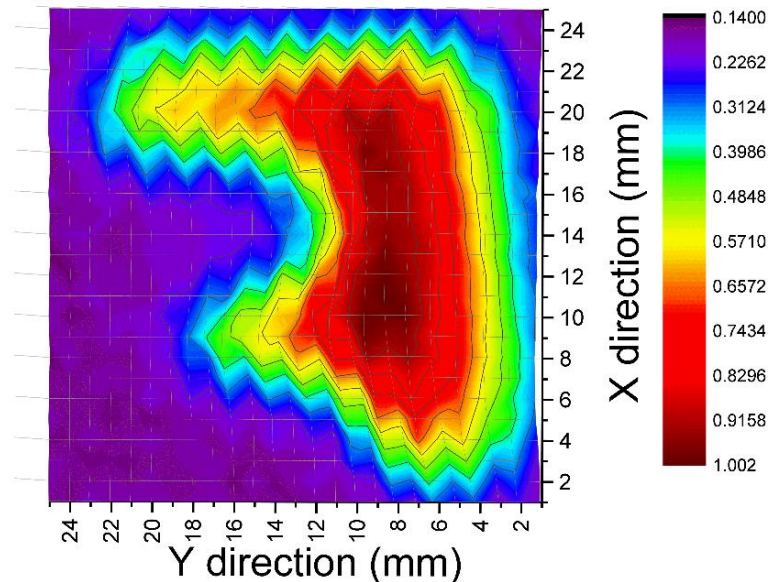


Figure 4.17: 24x24 pixel mm-wave images of the “F” shaped object obtained by the N523 GDD at the 87 GHz radiation frequency.

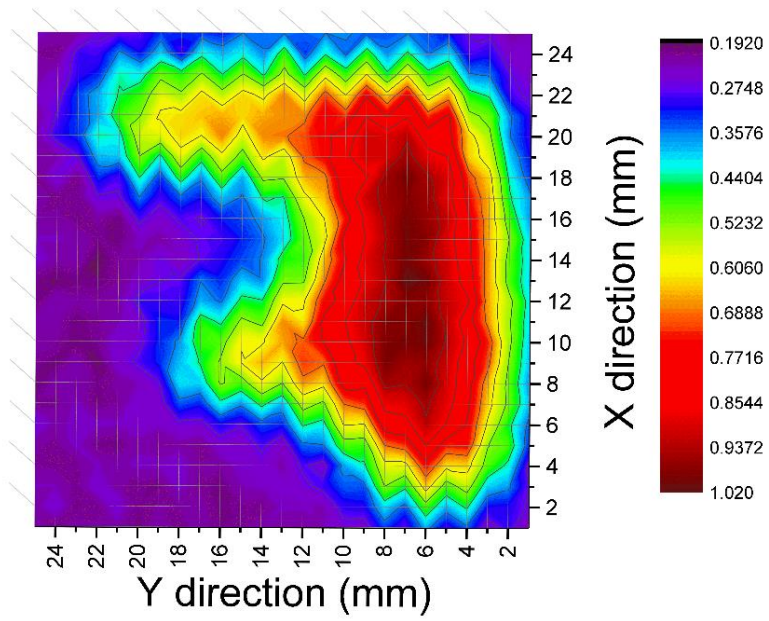


Figure 4.18: 24x24 pixel mm-wave images of the “F” shaped object obtained by the N523 GDD at the 100 GHz radiation frequency.

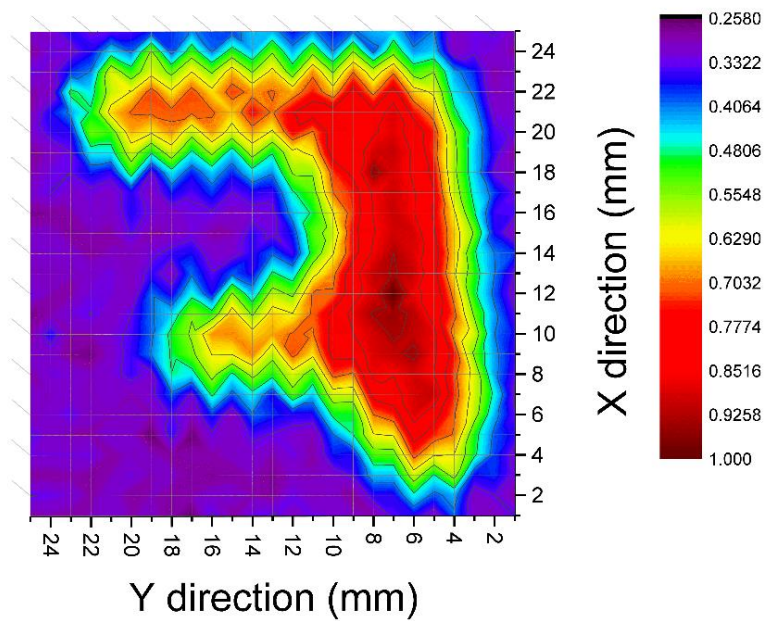


Figure 4.19: 24x24 pixel mm-wave images of the “F” shaped object obtained by the N523 GDD at the 119 GHz radiation frequency.

## CHAPTER 5

### CONCLUSION

In this thesis, two commercially available discharge lamps are characterized. First, the voltage-current characteristics of these GDDs are measured to investigate the glow mode. It is found that both GDDs are in the abnormal glow mode in which most of the atoms are in the excited and/or the ionized states. In order to determine the gas components, these GDDs are characterized using Optical Emission Spectroscopy (OES) method. It is found that the N520A discharge lamp consists of pure neon. On the other hand, the N523 contains Ne-Xe mixture. The electron temperature of the GDDs are measured using the Boltzmann method. The electron temperatures for the N523 GDD and N520A GDD are found as 0.42 eV and 0.28 eV at 9 mA discharge current, respectively.

The influence of the incident electromagnetic wave on the dc discharge plasma is studied. It is found that these low pressure GDDs are very sensitive to the millimeter wave radiation. The current in the discharge is slightly changed after exposing it to millimeter wave radiation which can be explained by the enhanced cascade ionization process. Special amplifier circuit is designed to measure the current change. The increase in the discharge current leads to an increase in the rate of the ionization and the electron density. In this case, more electrons are influenced by incident millimeter radiation. Thus the responsivity of both GDDs increase with increasing of the discharge current. The performance of N523 GDD as a millimeter wave detector is observed to be better than the performance of N520A GDD. The main physical difference between them, is found to be the gas type inside these lamps. Thus the penning effect has an important role in performance of the GDD. Using penning mixture of neon gases responsivity can be improved.

Moreover, the response of the GDDs strongly depend on the polarization of the incident radiation. The responsivity of the GDDs decrease with the increase in polarization angle difference between the electric fields of the discharge and the millimeter wave.

The N523 discharge lamp is employed as a single pixel detector for a cw millimeter wave active imaging system. The image is formed using raster scan method in which the object is moved using a programmable 2D-stage.

## REFERENCES

- [1] Tonouchi, M. (2007). Cutting-edge terahertz technology. *Nature Photonics*, 1(2), 97-105.
- [2] Rangan, S., Rappaport, T. S., & Erkip, E. (2014). Millimeter-wave cellular wireless networks: Potentials and challenges. *Proceedings of the IEEE*, 102(3), 366-385.
- [3] Luo, Q., Gao, S., & Zhang, L. (2015, May). Millimeter-wave smart antennas for advanced satellite communications. In *Microwave Symposium (IMS), 2015 IEEE MTT-S International* (pp. 1-4). IEEE.
- [4] Rojavin, M. A., & Ziskin, M. C. (1998). Medical application of millimeter waves. *QJM: monthly journal of the Association of Physicians*, 91(1), 57-66.
- [5] Mizuno, K., Matono, H., Wagatsuma, Y., Warashina, H., Sato, H., Miyanaga, S., & Yamanaka, Y. (2005, June). New applications of millimeter-wave incoherent imaging. In *Microwave Symposium Digest, 2005 IEEE MTT-S International* (pp. 4-pp). IEEE.
- [6] Appleby, R., & Wallace, H. B. (2007). Standoff detection of weapons and contraband in the 100 GHz to 1 THz region. *IEEE Transactions on Antennas and Propagation*, 55(11), 2944-2956.
- [7] Yujiri, L., Shoucri, M., & Moffa, P. (2003). Passive millimeter wave imaging. *IEEE Microwave Magazine*, 4(3), 39-50.
- [8] Lee, Y.-S. (2009). *Principles of Terahertz Science and Technology*. New York: Springer Science+Business Media.
- [9] Rogalski, A., & Sizov, F. (2011). Terahertz detectors and focal plane arrays. *Opto-Electronics Review*, 19(3), 346-404.
- [10] Raizer, Y.P. (1991). *Gas Discharge Physics*. Berlin: Springer-Verlag Berlin Heidelberg.
- [11] National Institute of Standards and Technology (NIST), NIST Atomic Spectra Database Ionization Energies Form. Retrieved from <https://physics.nist.gov/PhysRefData/ASD/ionEnergy.html>.

- [12] Chapman, B. (1980). *Glow Discharge Processes: Sputtering and Plasma Etching*. New York: Wiley.
- [13] Michaelson, H. B. (1977). The work function of the elements and its periodicity. *Journal of Applied Physics*, 48(11), 4729–4733.
- [14] Smirnov, B. M. (2015). *Theory of Gas Discharge Plasma*. Springer International Publishing Switzerland.
- [15] Townsend Discharge. Retrieved from [https://en.wikipedia.org/wiki/Townsend\\_discharge](https://en.wikipedia.org/wiki/Townsend_discharge).
- [16] Gordon, F. (1956). The Glow Discharge at Low Pressure. In S. Flügge, *Encyclopedia of Physics* (pp. 53-208). Springer Berlin Heidelberg.
- [17] Engel, A. v. (1994). *Ionized Gases*. American Institute of Physics.
- [18] Kunze, H.-J. (2009). *Introduction to Plasma Spectroscopy*. Springer-Verlag Berlin Heidelberg.
- [19] Asghar, H., Ali, R., & Baig, M. A. (2013). Determination of transition probabilities for the  $3p \rightarrow 3s$  transition array in neon using laser induced breakdown spectroscopy. *Physics of Plasmas*, 20(12), 123302.
- [20] Boogaard, A., Kovalgin, A. Y., Aarnink, A. A., Wolters, R. A., Holleman, J., Brunets, I., & Schmitz, J. (2006, November). Measurement of electron temperatures of Argon Plasmas in a High-Density Inductively-Coupled Remote Plasma System by Langmuir Probe and Optical-Emission Spectroscopy. In *Proceedings of the 9th annual workshop on Semiconductor Advances for Future Electronics and Sensors 2006*. Technology Foundation (STW).
- [21] Mahmood, S., Shaikh, N. M., Kalyar, M. A., Rafiq, M., Piracha, N. K., & Baig, M. A. (2009). Measurements of electron density, temperature and photoionization cross sections of the excited states of neon in a discharge plasma. *Journal of Quantitative Spectroscopy and Radiative Transfer*, 110(17), 1840-1850.
- [22] Griem, H. R. (1997). *Principles of Plasma Spectroscopy*. Cambridge: Cambridge University Press.
- [23] Gondal, M. A., Maganda, Y. W., Dastageer, M. A., Al Adel, F. F., Naqvi, A. A., & Qahtan, T. F. (2014). Detection of the level of fluoride in the commercially available toothpaste using laser induced breakdown spectroscopy with the marker atomic transition line of neutral fluorine at 731.1 nm. *Optics & Laser Technology*, 57, 32-38.

- [24] Moisan, M., & Pelletier, J. (2012). Individual motion of a charged particle in electric and magnetic fields. *In Physics of Collisional Plasmas* (pp. 101-202). Springer Netherlands.
- [25] Brown, S. C. (1968). *Introduction to Electrical Discharges in Gases*. John Wiley & Sons.
- [26] Kopeika, N. S. (1975). On the mechanism of glow discharge detection of microwave and millimeter-wave radiation. *Proceedings of the IEEE*, 63(6), 981-982.
- [27] Jackson, J. D. (1999). *Classical Electrodynamics*. John Wiley & Sons.
- [28] Vanderlinde, J. (2005). *Classical Electromagnetic Theory*. Springer Science+Business Media.
- [29] Kolner, B. H., Buckles, R. A., Conklin, P. M., & Scott, R. P. (2008). Plasma characterization with terahertz pulses. *IEEE Journal of Selected Topics in Quantum Electronics*, 14(2), 505-512.
- [30] Zheng, L., Zhao, Q., Liu, S., Xing, X., & Chen, Y. (2014). Theoretical and experimental studies of terahertz wave propagation in unmagnetized plasma. *Journal of Infrared, Millimeter, and Terahertz Waves*, 35(2), 187-197.
- [31] Zheng, L., Zhao, Q., Liu, S., Ma, P., Huang, C., Tang, Y., & Luo, X. (2012). Theoretical and experimental studies of 35 GHz and 96 GHz electromagnetic wave propagation in plasma. *Progress In Electromagnetics Research*, 24, 179-192.
- [32] Kopeika, N. S. (1978). Glow discharge detection of long wavelength electromagnetic radiation: Cascade ionization process internal signal gain and temporal and spectral response properties. *IEEE Transactions on Plasma Science*, 6(2), 139-157.
- [33] Farhat, N. H. (1974). Optimization of millimeter-wave glow-discharge detectors. *Proceedings of the IEEE*, 62(2), 279-281.
- [34] Hou, L., Park, H., & Zhang, X. C. (2011). Terahertz wave imaging system based on glow discharge detector. *IEEE Journal of Selected Topics in Quantum Electronics*, 17(1), 177-182.
- [35] Abramovich, A., Kopeika, N. S., Rozban, D., & Farber, E. (2007). Inexpensive detector for terahertz imaging. *Applied Optics*, 46(29), 7207-7211.
- [36] Rozban, D., Kopeika, N. S., Abramovich, A., & Farber, E. (2008). Terahertz detection mechanism of inexpensive sensitive glow discharge detectors. *Journal of Applied Physics*, 103(9), 093306.

- [37] Kopeika, N. S., & Rosenbaum, J. (1976). Subnormal Glow Discharge Detection of Optical and Microwave Radiation. *IEEE Transactions on Plasma Science*, 4(1), 51–61.
- [38] General Electric Company (1974). Fill gas mixture for glow lamps. US 3814971 A.
- [39] Ionascut-Nedelcescu, A., Carlone, C., Kogelschatz, U., Gravelle, D. V., & Boulos, M. I. (2008). Calculation of the gas temperature in a through flow atmospheric pressure dielectric barrier discharge torch by spectral line shape analysis. *Journal of applied physics*, 103(6), 063305.
- [40] Garamoon, A. A., Samir, A., Elakshar, F. F., Nosair, A., & Kotp, E. F. (2007). Spectroscopic study of argon DC glow discharge. *IEEE Transactions on Plasma Science*, 35(1), 1-6.
- [41] TeraOptronics B.V. (2013). Terahertz radiation detection using micro-plasma. US 2013/0256535 A1.
- [42] Alasgarzade, N., Nebioğlu, M. A., Takan, T., Uzun-Kaymak, I. U., Sahin, A. B., & Altan, H. (2017). Investigating Glow Discharge Detectors as a Millimeter-Wave/Terahertz Radiation Detection Tool. In *THz for CBRN and Explosives Detection and Diagnosis* (pp. 179-187). Springer, Dordrecht.
- [43] Takan, T., Alasgarzade, N., Uzun-Kaymak, I. U., Sahin, A. B., & Altan, H. (2016). Detection of far-infrared radiation using glow discharge detectors. *Optical and Quantum Electronics*, 48(5), 292.